Millimeter-wave spectroscopy and multichannel quantum-defect-theory analysis of high Rydberg states of xenon: The hyperfine structure of $^{129}Xe^+$ and $^{131}Xe^+$

Martin Schäfer, Matthias Raunhardt, and Frédéric Merkt*
Laboratory of Physical Chemistry, ETH Zurich, CH-8093 Zurich, Switzerland
(Received 24 November 2009; published 23 March 2010)

Millimeter-wave transitions between high-n Rydberg states of several isotopes of xenon have been recorded at sub-megahertz resolution. The fine and, for ^{129}Xe and ^{131}Xe, hyperfine structures of s, p, d, and f Rydberg states with principal quantum number in the range $52 \leqslant n \leqslant 64$ have been determined from combination differences and analyzed using multichannel quantum defect theory. Improved eigenquantum defects and channel interaction parameters for the odd- and even-parity Rydberg states of xenon and the hyperfine structure of the $^2P_{3/2}$ ground state of $^{129}Xe^+$ and $^{131}Xe^+$ have been obtained. Nearly degenerate p and d fine or hyperfine levels are very easily mixed by even weak stray electric fields.

DOI: 10.1103/PhysRevA.81.032514 PACS number(s): 32.10.Fn, 32.80.Ee, 32.30.Bv, 32.60.+i

I. INTRODUCTION

The determination of high-resolution spectroscopic information on cations represents a considerable challenge, particularly in cases where no allowed transitions lie in the infrared and visible regions of the electromagnetic spectrum. In such cases the information on the cation can be derived from Rydberg-state spectroscopy and extrapolation of the Rydberg series using multichannel quantum defect theory (MQDT) [1–3]. This method has been recently used to determine the hyperfine structure of the ground state of ortho-H_2^+ [4] and para-D_2^+ [5] and of both spin-orbit states ($^2P_{3/2}$ and $^2P_{1/2}$) of the ground state of $^{83}Kr^+$ [6–8]. For the two naturally occurring isotopes of xenon with nonzero nuclear spin, ^{129}Xe ($I = 1/2$) and ^{131}Xe ($I = 3/2$), the hyperfine structure of the $^2P_{1/2}$ state of the ion has been determined from the analysis of the autoionizing Rydberg series [9] (see Fig. 1); the determination of the hyperfine structure of the $^2P_{3/2}$ ground state of Xe^+ from high-resolution millimeter-wave spectra of high-n Rydberg states of xenon is the subject of this article.

We applied the same technique as was used to determine the hyperfine structure of the $^2P_{3/2}$ state of $^{83}Kr^+$ [6]: Millimeter-wave transitions between high-n Rydberg states of xenon were measured using selective field ionization and mass-selective detection of the ions; from the observed transition frequencies, the intervals between the Rydberg levels were derived with a precision of better than 1 MHz. The hyperfine structure of the ion was derived in a MQDT analysis of the millimeter-wave spectroscopic data together with complementary experimental data from the literature [9–57] (see Table I). Even though the millimeter-wave data cover only a small range of atomic energy levels, the high resolution makes it possible to determine accurate MQDT parameters which can be used to predict spectral positions over a substantial energy range, as already shown for krypton, where the MQDT parameters of the odd-parity states determined from the bound Rydberg states [6] also describe the autoionizing Rydberg states very well [8]. The presence of a nonzero nuclear spin I allows access to Rydberg states not accessible in $I = 0$ isotopes, and additional information is obtained from the hyperfine structure. Whereas the study of the hyperfine structure of the bound Rydberg states of krypton [6] covered only odd-parity states [the penetrating s ($\ell = 0$) and d ($\ell = 2$) Rydberg series with large quantum defects $\delta > 1$], this study includes even-parity p ($\ell = 1$) and f ($\ell = 3$) levels, of which the f states exhibit nonpenetrating character with small quantum defects ($0.02 \leqslant \delta \leqslant 0.06$). The new high-resolution millimeter-wave data enable us to improve the existing sets of MQDT data on xenon [43,57–65].

The quantum defects of p and d Rydberg states of xenon differ by almost exactly 1.0 (1.0007 for the $np[3/2]_1$ and $nd[1/2]_1$ Rydberg series) so that several hyperfine levels of moderately high ($n \sim 60$) Rydberg states are almost degenerate and can be mixed by small ($\mathcal{E} \sim 10$ mV/cm) electric stray fields. The high resolution of our millimeter-wave experiments allows us to study these effects and to observe, in the presence of a small stray field, otherwise forbidden transitions that are nominally $\Delta\ell = 0, \pm 2$. A simple model used to analyze these effects qualitatively and quantitatively is presented.

II. EXPERIMENTS

The millimeter-wave spectra of high-n Rydberg states of xenon were measured in an experiment similar to those described in Refs. [6,66]. The millimeter-wave source, a phase-stabilized backward wave oscillator (BWO) operating in the frequency range 240–380 GHz, has been described in Ref. [67]. In this study, the frequency range 240–348 GHz has been used.

Xenon atoms were excited to high Rydberg states in a $2 + 1'$ resonant three-photon process using UV and visible radiation from two pulsed dye lasers pumped by the tripled (355 nm) and doubled (532 nm) output of a neodymium-doped yttrium aluminum garnet (Nd:YAG) laser. The wave number of the first dye laser was doubled and set to correspond to the $(5p)^5(^2P_{3/2})6p[1/2]_0 \leftarrow (5p)^6\ ^1S_0$ two-photon resonance of xenon ($2\nu_1 = 80\,118.96$ cm^{-1}). The radiation of the second dye laser (17 670–17 676 cm^{-1}) further excited the xenon atoms to high ns and nd ($J = 1$) Rydberg states, which served as initial states for millimeter-wave transitions. To minimize the background ion signal (from $3\nu_1$ or $2\nu_1 + 2\nu_2$ photoionization), the powers of the lasers were set as low

*merkt@xuv.phys.chem.ethz.ch

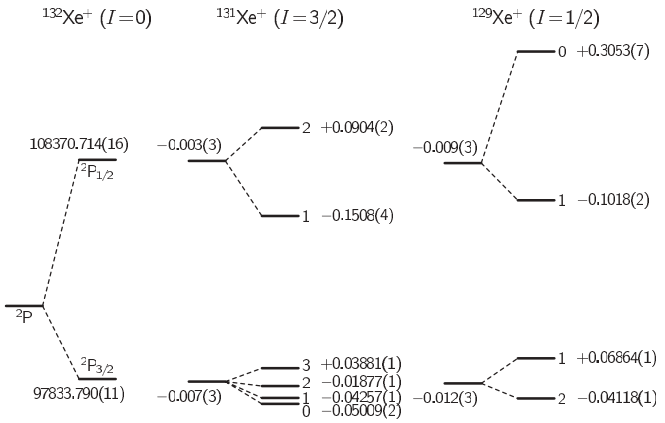

FIG. 1. Energy level diagram of the ^2P ground state of $^{132}Xe^+$, $^{131}Xe^+$, and $^{129}Xe^+$. For each spin-orbit component of the ion ($^2P_{3/2}$ and $^2P_{1/2}$), the wave numbers (per centimeter) of the ionization energies of ^{132}Xe from the $^1S_0$ ground state and the isotope shifts (per centimeter) for ^{131}Xe and ^{129}Xe are given. The hyperfine levels of $^{131}Xe^+$ and $^{129}Xe^+$ are labeled with the quantum number F^+, and their positions (per centimeter) with respect to the center of gravity of the hyperfine structure are given. The data for the $^2P_{1/2}$ state are from Ref. [9], the ionization energies for the $^2P_{3/2}$ state are from Ref. [48], and the hyperfine structures are determined in this article.

as possible, and the second laser was delayed with respect to the first one by about 15 ns using an optical delay line. Both laser beams were arranged collinearly and crossed a pulsed skimmed supersonic beam of xenon (Pangas, spectroscopic grade purity) at right angles in the middle of an array of resistively coupled cylindrical extraction plates. The millimeter-wave radiation entered the photoexcitation region perpendicularly to the xenon and the laser beams. Because an oversized waveguide is used for the BWO, its output is distributed among different electromagnetic modes with horizontal or vertical polarization [67]. The polarization vector of the first laser and the main polarization vector of the millimeter-wave radiation were oriented parallel to the atomic beam and the applied electric field; the polarization vector of the second laser and the secondary polarization vector of the millimeter-wave radiation were mutually perpendicular and perpendicular to the atomic beam and the applied field. This arrangement allows the observation of $\Delta M_F = 0, \pm 1$ transitions and does not lead to any polarization restriction of the observable millimeter-wave transitions.

The millimeter-wave transitions were detected by selective field ionization using a pulsed electric field in the range between 40 and 133 V/cm, which was applied 1–4 μs after the laser pulse and also accelerated the xenon ions toward a microchannel plate detector. Spectra of different xenon isotopes (^{128}Xe, ^{129}Xe, ^{130}Xe, ^{131}Xe, ^{132}Xe, ^{134}Xe, and ^{136}Xe) were recorded by placing temporal gates at the corresponding positions of the time-of-flight (TOF) spectrum. Examples of such isotope-selective spectra are displayed in Figs. 2 and 3. The photoexcitation region and the adjacent TOF tube were surrounded by two cylindrical mu-metal shields to minimize stray magnetic fields. The residual stray electric fields were reduced to values below 5 mV/cm using the procedure described in Ref. [68], which consisted of measuring the quadratic Stark shift for different applied fields and determining the field for which the Stark shift was minimal (see Fig. 4). To avoid power broadening of the millimeter-wave transitions (cf. Ref. [66]),

TABLE I. Overview of the experimental energy levels reported in the literature.

$n\ell\,[K]_J$	n	Refs.	$n\ell\,[K]_J$	n	Refs.
$nd[1/2]_0$	5–21	[15,26,43,49]	$np[1/2]_0$	6–42	[15,36,49,54]
$ns'[1/2]_0$	6–7, 9–15	[15,32,49]	$np'[1/2]_0$	6–11, 13, 18–31	[15,24,34,41,49,51]
$nd[1/2]_1$	5–34	[15,26,27,48,49]	$np[1/2]_1$	6–12, 15–19, 28–40	[15,24,29,49]
$nd[3/2]_1$	5–66	[15,26,27,48,49]	$np[3/2]_1$	6–12	[15,49]
$ns[3/2]_1$	6–47	[15,26,27,49]	$nf[3/2]_1$	4–73	[15,24,29,49]
$nd'[3/2]_1$	5–78	[14,15,23,27,28,32,39,45,49]	$np'[3/2]_1$	6–17	[15,24,31,42,49,51,55]
$ns'[1/2]_1$	6–52	[14,15,23,27,28,32,39,45,48,49]	$np'[1/2]_1$	6–17	[15,24,31,42,49,51,55]
$nd[3/2]_2$	5–25	[15,26,49]	$np[5/2]_2$	6–27	[15,36,49]
$nd[5/2]_2$	5–25	[15,26,49]	$np[3/2]_2$	6–27	[15,36,49]
$ns[3/2]_2$	6–44	[15,26,43,49]	$nf[3/2]_2$	4–19[a]	[15,36,43,49]
$nd'[3/2]_2$	5, 7–40	[32,49,50]	$nf[5/2]_2$	4–19[a]	[15,36,43,49]
$nd'[5/2]_2$	5, 7–24	[32,49,50,57]	$np'[3/2]_2$	6–11, 13	[15,24,41,49,51,55]
$nd[7/2]_3$	5–25	[15,26,49]	$nf'[5/2]_2$	4–13	[24,41,44,49]
$nd[5/2]_3$	5–29	[15,26,43,49]	$np[5/2]_3$	6–15	[15,49]
$nd'[5/2]_3$	5, 7–40	[15,32,49,50,57]	$nf[5/2]_3$	4–11	[15,49]
$nd[7/2]_4$	5–44	[15,26,43,49]	$nf[7/2]_3$	4–13	[15,43,49]
			$nf'[7/2]_3$	4–8[b]	[49,55]
			$nf'[5/2]_3$	4–8[b]	[49]
			$nf[9/2]_4$	4–11	[15,49]
			$nf[7/2]_4$	4–9	[15,49]
			$nf'[7/2]_4$	4–8[b]	[41,49,55]
			$nf[9/2]_5$	4–11	[15,49]

[a]The $nf[3/2]_2$ and $nf[5/2]_2$ levels with $n > 19$ are not resolved in the experiments reported in Ref. [36].

[b]Of the autoionizing $nf'[K]_J (J = 3, 4)$ Rydberg series, only the $n = 4, 5$ levels of the $K = 7/2 (J = 3, 4)$ series reported in Ref. [55] and the $n = 4 - 7$ levels of $nf'[7/2]_5$ in Ref. [41] are resolved.

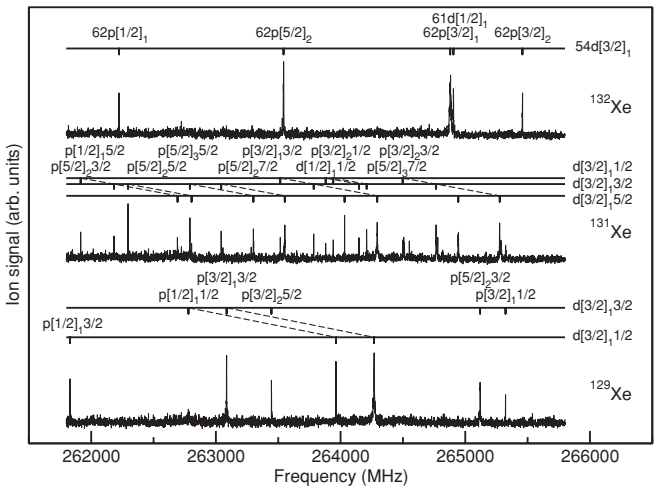

FIG. 2. Comparison of millimeter-wave overview spectra of the $62p \leftarrow 54d[3/2]_1$ transitions for the three most abundant isotopes: (top) ^{132}Xe ($I = 0$, 26.9% nat. abundance), (middle) ^{131}Xe ($I = 3/2$, 21.2%), and (bottom) ^{129}Xe ($I = 1/2$, 26.4%). For ^{129}Xe and ^{131}Xe, the marks on the assignment bars for transitions sharing the same final state are connected by thin dashed lines for easier interpretation. The spacing between the assignment bars represents the hyperfine structure of the intermediate $54d[3/2]_1$ state.

the millimeter-wave radiation was attenuated by about -10 dB by introducing stacks of paper between the millimeter-wave source and the experimental chamber. These measures allowed an accuracy in the measured transition frequencies of better than 1 MHz.

III. MQDT CALCULATIONS

To analyze the Rydberg spectrum of Xe using MQDT, we follow the formalism introduced by Lu [58] and Lee and Lu [69] for the analysis of the Xe and Ar absorption spectra. This formalism was extended by Wörner *et al.* [7,9] (in a method similar to that outlined by Sun [70]) for the analysis of the hyperfine structure of ^{83}Kr and of the autoionizing Rydberg states of ^{129}Xe and ^{131}Xe and was used to analyze the millimeter-wave spectra of ^{83}Kr [6].

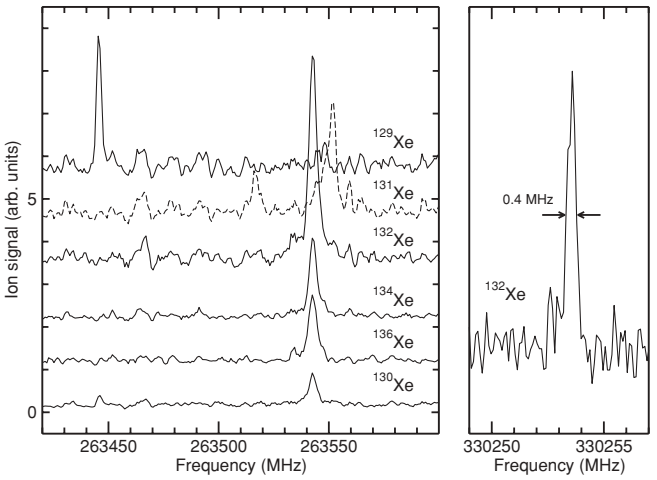

FIG. 3. (left) Section of the millimeter-wave overview spectrum of the $62p[5/2]_2 \leftarrow 54d[3/2]_1$ transition of xenon recorded in different mass channels. The spectra have been shifted along the vertical axis by an offset of 0–5 arb. units. The spectrum of the ^{131}Xe isotope is drawn with a dashed line, and the ^{130}Xe spectrum is placed at the bottom for clarity. The strong peak in the ^{129}Xe spectrum at 263 445.7 MHz is the $62p[3/2]_2(5/2) \leftarrow 54d[3/2]_1(3/2)$ transition, the strong peak in the ^{131}Xe spectrum at 263 552.7 MHz is the $62p[5/2]_3(5/2) \leftarrow 54d[3/2]_1(5/2)$ transition, and the weak peak at 263 516.4 MHz is the $62p[3/2]_1(3/2) \leftarrow 54d[3/2]_1(1/2)$ transition. (right) Millimeter-wave spectrum of the $61p[5/2]_2 \leftarrow 52d[3/2]_1$ transition of ^{132}Xe at high resolution.

Three different angular momentum coupling schemes are used. In the close-coupling region of the electron-ion collision, the electrostatic interaction between the electron and the ion core is larger than the spin-orbit interaction and much larger than the hyperfine interaction [69]. Therefore the following (LS) angular momentum coupling scheme is adequate to describe the close-coupling eigenchannels:

$$\vec{L}^+ + \vec{\ell} = \vec{L}, \quad \vec{S}^+ + \vec{s} = \vec{S}, \quad \vec{L} + \vec{S} = \vec{J}, \quad \vec{J} + \vec{I} = \vec{F}, \tag{1}$$

where $\vec{L}^+$ and $\vec{S}^+$ represent the orbital and spin angular momenta of the ionic core, $\vec{\ell}$ and $\vec{s}$ represent the corresponding

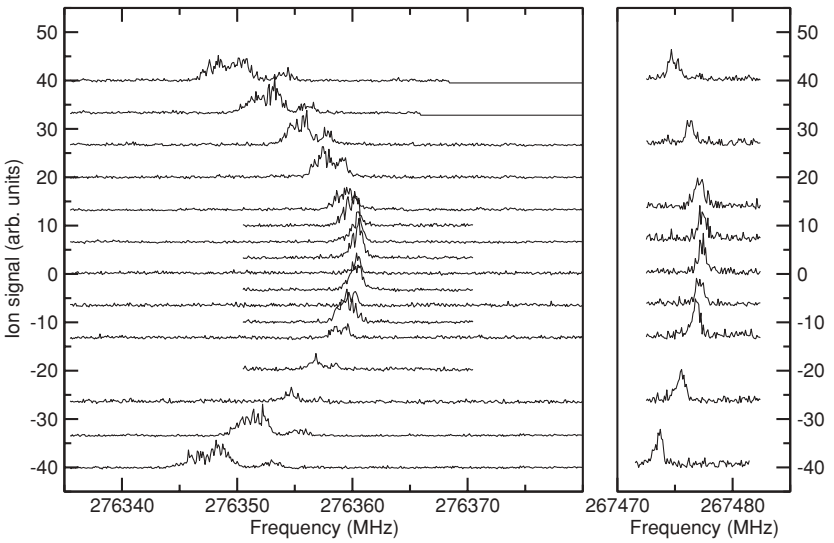

FIG. 4. Millimeter-wave transitions between Rydberg states of ^{132}Xe in the presence of different electric fields. The spectra are shifted along the vertical axis by an offset corresponding to the value of the applied field in millivolts per centimeter (from -40 mV/cm to $+40$ mV/cm). The $57f[3/2]_2 \leftarrow 53d[1/2]_1$ transition with a field-free transition frequency of 276 360.5 MHz (left) exhibits a stronger Stark effect than the $61p[5/2]_2 \leftarrow 55s[3/2]_1$ transition at 267 477.3 MHz (right) and is split into different $M'_J \leftarrow M''_J$ components, of which the $|M'_J| = 1 \leftarrow |M''_J| = 1$ component should be the strongest according to the ΔM_J selection rules.

TABLE II. Summary of the total angular momentum quantum number F of the hyperfine Rydberg levels converging to each hyperfine state F^+ of the ion. The last two lines represent the case $I = 0$, where $F^+ = J^+$ and $F = J$.

	$\ell = 0$	$\ell = 1$		$\ell = 2$		$\ell = 3$	
F^+	$j = 1/2$	$j = 1/2$	$j = 3/2$	$j = 3/2$	$j = 5/2$	$j = 5/2$	$j = 7/2$
0	1/2	1/2	3/2	3/2	5/2	5/2	7/2
1	1/2, 3/2	1/2, 3/2	1/2–5/2	1/2–5/2	3/2–7/2	3/2–7/2	5/2–9/2
2	3/2, 5/2	3/2, 5/2	1/2–7/2	1/2–7/2	1/2–9/2	1/2–9/2	3/2–11/2
3	5/2, 7/2	5/2, 7/2	3/2–9/2	3/2–9/2	1/2–11/2	1/2–11/2	1/2–13/2
1/2	0, 1	0, 1	1, 2	1, 2	2, 3	2, 3	3, 4
3/2	1, 2	1, 2	0–3	0–3	1–4	1–4	2–5

angular momenta of the Rydberg electron, and $\vec{I}$ represents the nuclear spin. In the long-range part of the electron-ion collision, however, the energy level structure of the Rydberg states corresponds primarily to the energy levels of the ionic core. Thus the following $(F^+ j)$ coupling scheme (or $J^+ j$ for isotopes with zero nuclear spin) is used for the dissociation (or fragmentation) channels [7]:

$$\vec{L}^+ + \vec{S}^+ = \vec{J}^+, \quad \vec{J}^+ + \vec{I} = \vec{F}^+, \quad \vec{\ell} + \vec{s} = \vec{j}, \quad \vec{F}^+ + \vec{j} = \vec{F}. \tag{2}$$

An overview of all possible hyperfine levels with $\ell \leqslant 3$ is given in Table II. The assignments of the Rydberg levels observed in this study are made using the notation $n\ell\,[K]_J(F)$ based on the traditional Racah $(J^+\ell)$ coupling scheme [71]:

$$\vec{L}^+ + \vec{S}^+ = \vec{J}^+, \quad \vec{J}^+ + \vec{\ell} = \vec{K}, \quad \vec{K} + \vec{s} = \vec{J}, \quad \vec{J} + \vec{I} = \vec{F}. \tag{3}$$

Table I summarizes all $n\ell\,[K]_J$ Rydberg series with $\ell \leqslant 3$ observed so far; a prime indicates, as usual, Rydberg states belonging to series converging to the $^2P_{1/2}$ ionization limit.

For atoms with a nuclear spin $I = 0$, the energies of the bound states are well described by a set of MQDT parameters consisting of the ionization thresholds $E_i \equiv E(^2P_{J^+})$, the eigenchannel quantum defects μ_α, their energy dependence, and the elements of the orthogonal transformation matrix $U_{i\alpha}$ connecting the close-coupling eigenchannels α to the fragmentation channels i. Each bound energy level is represented by two effective principal quantum numbers $\nu_{3/2}$ and $\nu_{1/2}$, defined by the relations

$$E = E\left(^2P_{3/2}\right) - \frac{hcR_M}{(\nu_{3/2})^2} = E\left(^2P_{1/2}\right) - \frac{hcR_M}{(\nu_{1/2})^2}, \tag{4}$$

where the mass-dependent Rydberg constant R_M is defined as $R_M = R_\infty M^+/M$, with the atomic mass M and the ionic mass $M^+ = M - m_e$. The bound energy levels are the solutions satisfying the relation

$$\sum_\alpha U_{i\alpha} \sin[\pi(\nu_i + \mu_\alpha)] A_\alpha = 0, \tag{5}$$

which has nontrivial solutions when

$$\det |U_{i\alpha} \sin[\pi(\nu_i + \mu_\alpha)]| = 0. \tag{6}$$

In Eqs. (5) and (6), ν_i is defined with respect to the corresponding ionization limit according to Eq. (4), and A_α is the expansion coefficient of the radial part of the Rydberg electron wave function in the basis of the close-coupling eigenchannels. The elements $U_{i\alpha}$ of the $N \times N$ transformation matrix are conveniently factorized as

$$U_{i\alpha} = \sum_{\tilde{\alpha}} U_{i\tilde{\alpha}} V_{\tilde{\alpha}\alpha}, \tag{7}$$

where $U_{i\tilde{\alpha}} = \langle LSJ|J^+ jJ\rangle$ represents elements of the $J^+ j$-LS frame-transformation matrix. $V_{\tilde{\alpha}\alpha}$ accounts for the typically small departure of the close-coupling channels from pure LS coupling and may be represented by $N(N-1)/2$ generalized Euler angles θ_{jk}, as described by Lee and Lu [69]:

$$V_{\tilde{\alpha}\alpha} = \prod_j^N \prod_{k>j}^N \boldsymbol{R}(\theta_{jk}) = \boldsymbol{R}(\theta_{12}) \cdot \boldsymbol{R}(\theta_{13}) \cdot \cdots \cdot \boldsymbol{R}(\theta_{23}) \cdot \cdots, \tag{8}$$

where $\boldsymbol{R}(\theta_{jk})$ are rotation matrices defined as

$$R_{mm}(\theta_{jk}) = \begin{cases} \cos\theta_{jk} & \text{if} \quad m = j \text{ or } m = k \\ 1 & \text{otherwise} \end{cases},$$

$$R_{mn}(\theta_{jk}) = \left\{ \begin{cases} -\sin\theta_{jk} & \text{if} \quad m = j, n = k \\ \sin\theta_{jk} & \text{if} \quad m = k, n = j \\ 0 & \text{otherwise} \end{cases} \right\} m \neq n. \tag{9}$$

The energy dependence of μ_α can be approximated by

$$\mu_\alpha = \mu_\alpha^0 + \epsilon\,\mu_\alpha^1, \tag{10}$$

where

$$\epsilon = \frac{E - E(^2P_{3/2})}{hcR_M} \text{ or } \epsilon = -(\nu_{3/2})^{-2} \quad (\text{for } \epsilon < 0). \tag{11}$$

Because the hyperfine interaction in the ionic core is much smaller than the spin-orbit interaction, which leads to a level separation of 10 536.92 cm^{-1} between the $^2P_{3/2}$ and $^2P_{1/2}$ levels [9], mixing of the spin-orbit components by the hyperfine interaction is negligible. Therefore the hyperfine structures of the two spin-orbit components (see Fig. 1) can be treated separately and expressed as functions of the magnetic dipole and electric quadrupole hyperfine coupling constants A_{J^+} and B_{J^+} [$B_{J^+} = 0$ for $I = 1/2$ (^{129}Xe) or $J^+ = 1/2$] as

$$\frac{E(J^+, F^+)}{hc} = \frac{E(J^+)}{hc} + A_{J^+}\frac{C}{2} + B_{J^+}\frac{\frac{3}{4}C(C+1) - I(I+1)J^+(J^+ + 1)}{2I(2I-1)J^+(2J^+ - 1)}, \tag{12}$$

where $C = F^+(F^+ + 1) - I(I + 1) - J^+(J^+ + 1)$ and $E(J^+)$ is the energy of the center of gravity of the hyperfine structure. The contribution from the octupole coupling is many orders of magnitude smaller [12,72] and thus neglected here. In analogy to Eq. (6), the Rydberg levels are determined by solving the determinantal equation

$$\det |U_{i_F\alpha_F} \sin[\pi(\nu_{i_F} + \mu_{\alpha_F})]| = 0, \tag{13}$$

where

$$U_{i_F\alpha_F} = \sum_{\bar{\alpha}_F} U_{i_F\bar{\alpha}_F} V_{\bar{\alpha}_F\alpha_F}, \tag{14}$$

and ν_{i_F} is an effective principal quantum number $\nu_{J^+F^+}$ defined relative to the position of the ionization threshold $E_{i_F} \equiv E(^2P_{J^+F^+})$ of the dissociation channel i_F (i.e., the position of one of the four or six hyperfine levels of the ion):

$$E = E(^2P_{J^+F^+}) - \frac{hcR_M}{(\nu_{J^+F^+})^2}. \tag{15}$$

The elements of the frame-transformation matrix $U_{i_F\bar{\alpha}_F} = \langle LSJF|J^+F^+jF\rangle$ are calculated as [6,7]

$$\begin{aligned}\langle LSJF|J^+F^+jF\rangle = {} & (2F+1)\sqrt{(2J+1)(2L+1)(2S+1)(2j+1)(2F^++1)(2J^++1)} \\ & \times \sum_{m_j,m_{J^+},m_J,m_\ell,m_{L^+},m_L,m_s,m_{S^+},m_S,m_{F^+},m_I} (-1)^{F^+-j-J^++2I-J+L-S-2s+3m_F+m_{J^+}+2m_J} \\ & \times \begin{pmatrix} I & J & F \\ m_I & m_J & -m_F \end{pmatrix} \begin{pmatrix} L & S & J \\ m_L & m_S & -m_J \end{pmatrix} \begin{pmatrix} L^+ & \ell & L \\ m_{L^+} & m_\ell & -m_L \end{pmatrix} \begin{pmatrix} S^+ & s & S \\ m_{S^+} & m_s & -m_S \end{pmatrix} \\ & \times \begin{pmatrix} F^+ & j & F \\ m_{F^+} & m_j & -m_F \end{pmatrix} \begin{pmatrix} \ell & s & j \\ m_\ell & m_s & -m_j \end{pmatrix} \begin{pmatrix} I & J^+ & F^+ \\ m_I & m_{J^+} & -m_{F^+} \end{pmatrix} \begin{pmatrix} L^+ & S^+ & J^+ \\ m_{L^+} & m_{S^+} & -m_{J^+} \end{pmatrix}\end{aligned} \tag{16}$$

for any value of m_F. Whereas the frame-transformation matrix $U_{i\alpha}$ for $I = 0$ isotopes is block-diagonal in J, the transformation matrix $U_{i_F\alpha_F}$ can be separated into individual F blocks, of which the even-parity $F = 5/2$ matrix of ^{131}Xe, with dimension 19×19, is the largest. The dimensions of the $U_{i\alpha}$ and $U_{i_F\alpha_F}$ matrices can be easily derived from Table II, which summarizes all s, p, d, and f Rydberg series of xenon, including hyperfine structure. Assuming that the eigenchannel quantum defects μ_α are equal for all isotopes and that the hyperfine interaction is negligible in the close-coupling region, the eigenchannel quantum defects μ_α obtained from the analysis of the Rydberg levels of any given $I = 0$ isotope and the corresponding $V_{\bar{\alpha}\alpha}$ matrix elements can also be used for the analysis of $I > 0$ isotopes, that is, $\mu_{\alpha_F} = \mu_\alpha$ and $V_{\bar{\alpha}_F\alpha_F} = V_{\bar{\alpha}\alpha}$. The signs of the elements of the corresponding frame-transformation matrices of the different J values must be consistent, which can be ensured by calculating the elements $U_{i\bar{\alpha}} = \langle LSJ|J^+jJ\rangle$ with Eq. (16) and setting $I = 0$ (in which case, $F^+ = J^+$ and $F = J$). Several of the $U_{i\bar{\alpha}}$ matrix elements have a different sign than in Refs. [73,74].

Above the $^2P_{3/2}$ ionization threshold, the boundary condition for the dissociation channels which remain closed ($i \in Q$) is still described by Eq. (5). The dissociation channels that are open ($i \in P$) are required to have a common eigenphase shift $\pi\tau$:

$$\sum_\alpha U_{i\alpha} \sin[\pi(-\tau + \mu_\alpha)]A_\alpha = 0. \tag{17}$$

This system of equations can be put into the standard form of a generalized eigenvalue problem for $\tan(\pi\tau)$ [75]:

$$\mathbf{\Gamma A} = \tan(\pi\tau)\mathbf{\Lambda A}, \tag{18}$$

with

$$\Gamma_{i_F\alpha_F} = \begin{cases} U_{i_F\alpha_F} \sin\left[\pi\left(\nu_{i_F} + \mu_{\alpha_{(F)}}\right)\right] & \text{for } i_F \in Q, \\ U_{i_F\alpha_F} \sin\left[\pi\mu_{\alpha_{(F)}}\right] & \text{for } i_F \in P, \end{cases} \tag{19}$$

$$\Lambda_{i_F\alpha_F} = \begin{cases} 0 & \text{for } i_F \in Q, \\ U_{i_F\alpha_F} \cos\left[\pi\mu_{\alpha_{(F)}}\right] & \text{for } i_F \in P. \end{cases} \tag{20}$$

This eigenvalue problem has as many solutions (τ_ρ and expansion coefficients $\boldsymbol{A}^\rho$) as there are open channels. The total photoionization cross section is

$$\sigma(\omega) \propto \omega \sum_F \frac{2F+1}{2F_0+1} \sum_\rho \frac{1}{N_\rho} \left(\sum_{\alpha_{(F)}} D_{\alpha_{(F)}} A^\rho_{\alpha_{(F)}} \right)^2, \tag{21}$$

where ω is the photon energy, F_0 is the total angular momentum quantum number of the initial state, D_α is the reduced dipole matrix element, and the normalization factor N_ρ is given by

$$N_\rho^2 = \sum_{i_F \in P} \left\{ \sum_{\alpha_{(F)}} U_{i_F\alpha_F} \cos\left[\pi\left(-\tau_\rho + \mu_{\alpha_{(F)}}\right)\right] A^\rho_{\alpha_{(F)}} \right\}^2. \tag{22}$$

IV. RESULTS

Typical millimeter-wave overview spectra are shown in Fig. 2. The spectra correspond to transitions from the $54d[3/2]_1(F)$ Rydberg state to $62p[K]_J(F')$ Rydberg states of xenon and cover a range of 4 GHz (0.13 cm^{-1}). Recording spectra of different isotopes simultaneously by setting several temporal gates at the corresponding positions of the TOF

TABLE III. Rydberg states of ^{132}Xe observed by millimeter-wave spectroscopy. The energies/h (megahertz) are relative to the position of the $52d[1/2]_1$ level. The differences between observed and calculated (MQDT) energies $(E_o - E_c)/h$ (megahertz) are given in brackets. The position of the $52d[1/2]_1$ level of ^{132}Xe above the $^1S_0$ ground state is 97 788.973(11) cm^{-1}, as derived from the MQDT analysis. The last column gives the effective quantum defects δ of the observed Rydberg states; the numbers in parentheses represent 1 standard deviation in units of the last digit.

$n\ell\,[K]_J$						δ
	$n = 57$	$n = 58$	$n = 59$	$n = 60$	$n = 61$	
$(n+4)s[3/2]_1$		365 834[−0.3]		429 925[−0.5]		
$nf[5/2]_2$	329 949.9[0.2]	364 619.5[−0.1]	397 540.3[−0.2]	428 828.5[0.1]	458 589[−0.5]	0.03018(12)
$nf[3/2]_2$	329 062.4[0.2]	363 777.5[0.3]	396 740.2[−0.1]	428 067.6[0.1]	457 865[−0.1]	0.05509(12)
$nf[3/2]_1$	328 957.8[0.2]	363 677.8[0.1]	396 645.6[−0.1]	427 977.6[0.1]	457 779[−0.3]	0.05804(12)
$(n+3)p[1/2]_0$			384 395[0.3]	416 332[0.3]	446 700[0.3]	3.43567(14)
$(n+2)d[3/2]_2$		349 416[0.0]	383 100[0.1]	415 101[0.3]		2.47516(13)
$(n+3)p[3/2]_2$	313 003.8[−0.2]	348 539.2[−0.1]	382 267.2[−0.8]	414 309.5[−0.9]		3.50050(12)
$(n+2)d[1/2]_1$	312 389.4[1.0]	347 956.1[1.3]	381 713.6[1.1]	413 783.5[1.4]		2.51734(12)
$(n+3)p[3/2]_1$	312 362.8[−1.0]	347 931.3[−0.5]	381 689.6[−1.4]	413 760.4[−1.6]		3.51807(12)
$(n+3)p[5/2]_2$	310 876.6[−0.2]	346 521.0[0.1]	380 351.4[0.4]	412 488.7[0.6]		3.55872(12)
$(n+3)p[1/2]_1$	309 412.7[−0.2]	345 131.8[−0.4]	379 032.4[0.3]	411 235.2[0.6]		3.59870(12)
	$n = 50$	$n = 51$	$n = 52$	$n = 53$		
$(n+4)s[3/2]_1$	27 961.9[−0.3]	79 043.8[−0.3]	127 207.4[−0.3]			3.99423(8)
$(n+2)d[3/2]_1$	16 267.5[0.2]	68 022.6[0.0]	116 809.1[0.4]	162 849.0[0.1]		2.21505(8)
$(n+2)d[1/2]_1$	0.0[0.1]	52 702.1[0.3]	102 362.8[−0.1]	149 212.1[−0.1]		2.51732(8)

spectrum is very efficient and enables the detection of even weak transitions. The shifts of isotopes with even mass numbers are negligible, thus the transitions between high Rydberg states are observed at almost the same frequencies for all $I = 0$ isotopes but at different frequencies for the $I \neq 0$ isotopes because of the hyperfine splittings (see Fig. 3).

Transitions have been assigned using combination differences and the general $\Delta F = 0, \pm 1$ selection rule ($\Delta J = 0, \pm 1$ for $I = 0$ isotopes). Electric dipole transitions are expected to occur between states of opposite parity and follow the $\Delta\ell = \pm 1$ selection rule. The latter does not strictly hold because transitions between s and f Rydberg states could be observed for all isotopes as a result of the mixing of s and d eigenchannels. Indeed, transitions to states of all $np[K]_J$ and $nf[K]_J$ Rydberg series of ^{132}Xe with $J = 1, 2$ have been observed not only from the intermediate $nd[1/2]_1$ and $nd[3/2]_1$ Rydberg states but also from the $ns[3/2]_1$ states.

For ^{132}Xe with $I = 0$, effective quantum defects $\delta = n - \nu_{3/2}$ have been obtained for the $n\ell\ [K]_J$ series from a fit to the observed transition frequencies and are given in Table III. The quantum defects are almost constant for the observed levels, except for the $nd[3/2]_1$ series, for which the quantum defect increases with increasing energy. These quantum defects allowed us to assign the transitions located in the immediate vicinity of the (power-broadened) transitions to $np[3/2]_1$ Rydberg states to transitions to $(n-1)d[1/2]_1$ Rydberg states (see Figs. 2 and 5). These transitions are forbidden according to the $\Delta\ell = \pm 1$ and $+ \leftrightarrow -$ parity selection rules for electric dipole transitions but become allowed in the presence of residual electric fields, which mix the nearly degenerate ($\Delta\nu_{3/2} = 0.0007$) $np[3/2]_1$ and $(n-1)d[1/2]_1$ Rydberg states (see the following discussion). The assignment is corroborated by the fact that the transition disappears when the stray electric fields are minimized. "Forbidden" $n's[3/2]_1 \leftarrow nd[1/2]_1$ and $n'd[3/2]_2 \leftarrow nd[1/2]_1$ transitions have been observed and assigned as well.

The positions of the observed Rydberg levels of ^{132}Xe, ^{129}Xe, and ^{131}Xe relative to the positions of the $52d[1/2]_1$, $52d[1/2]_1(3/2)$, and $52d[1/2]_1(5/2)$ levels, respectively, could be determined with an accuracy better than 1 MHz by fitting the relative level energies to the observed transition frequencies in a least squares fit, the results of which are presented in Tables III–V. Some levels could only be observed

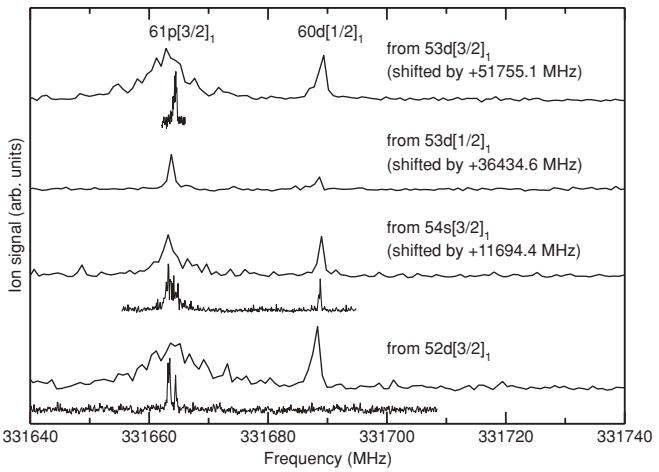

FIG. 5. Millimeter-wave spectra exhibiting transitions from selected nd and ns initial states to the $61p[3/2]_1$ and $60d[1/2]_1$ Rydberg states of ^{132}Xe. Transitions from d or s states to d Rydberg states are forbidden by the $\Delta\ell$ selection rule but become allowed in the presence of electric fields. High-resolution spectra recorded with reduced millimeter-wave power are presented below the low-resolution overview spectra. The transitions to the $60d[1/2]_1$ state disappeared after minimization of the stray electric field, as shown in the bottom spectrum.

TABLE IV. Rydberg states of ^{129}Xe observed by millimeter-wave spectroscopy. The energies/h (megahertz) are relative to the position of the $52d[1/2]_1(3/2)$ level. The differences between observed and calculated energies $(E_o - E_c)/h$ (megahertz) are given in brackets. The position of the $52d[1/2]_1(3/2)$ level of ^{129}Xe above the $^1S_0$ $(F = 1/2)$ ground state is 97 788.938(11) cm^{-1}.

$n\ell\,[K]_J$	F					
		$n = 57$	$n = 58$	$n = 59$	$n = 60$	$n = 61$
$nf[7/2]_3$	5/2			400 452[0.1]	431 731[0.2]	461 483[−0.3]
$nf[5/2]_3$[a]	5/2		366 865[−0.4]	399 807.6[−0.4]	431 116[0.0]	460 897[−0.5]
$nf[5/2]_2$	3/2	332 129.7[0.4]	366 823[−0.4]	399 767.0[0.0]	431 076.4[0.0]	460 858[0.4]
$nf[5/2]_2$[a]	5/2	329 481.6[0.2]	364 146.4[0.0]	397 062.3[−0.8]	428 346[−0.3]	458 104[−0.4]
$nf[3/2]_1$[a]	3/2	328 951.0[0.2]	363 646.2[−0.1]	396 590.7[0.0]	427 901.2[0.7]	457 682[0.2]
$nf[3/2]_2$	5/2	328 912.3[−0.3]	363 608.4[−0.3]	396 553.3[−0.8]	427 864[−0.2]	
$nf[3/2]_2$[a]	3/2	328 484.0[0.5]	363 199.8[0.8]	396 163.1[0.4]	427 491.2[0.8]	457 290[1.3]
$nf[3/2]_1$	1/2	328 392[1.1]	363 111.6[0.1]	396 079.8[0.3]	427 411.6[0.2]	457 214[0.4]
$(n+3)p[1/2]_0$	1/2			385 852[0.0]	417 822[0.1]	448 224[0.2]
$(n+3)p[3/2]_2$	3/2	315 457[0.4]	351 000[0.0]	384 736[−0.9]	416 786[−0.6]	447 260[−1.1]
$(n+3)p[5/2]_3$[a]	5/2	314 571[0.7]	350 160[0.7]	383 938[0.2]	416 029[1.2]	446 541[1.0]
$(n+3)p[3/2]_1$	1/2	314 019[0.2]	349 586.4[−0.5]	383 347.6[−0.2]	415 421.9[−0.4]	445 922[0.5]
$(n+3)p[5/2]_2$[a]	3/2	313 686.3[−0.2]	349 321.2[−0.4]	383 144.1[0.2]	415 274.9[0.6]	445 825[0.7]
$(n+2)d[3/2]_2$	5/2		349 332.1[−0.5]		414 990[−1.0]	445 405[−1.1]
$(n+2)d[1/2]_1$	3/2		347 828[0.8]	381 571.6[0.6]	413 628.0[1.0]	
$(n+3)p[3/2]_2$[a]	5/2	312 170.9[−0.5]	347 725.4[−1.2]	381 471.2[−1.9]	413 529.7[−1.6]	
$(n+3)p[3/2]_1$[a]	3/2	311 772.2[−0.3]	347 346.4[−0.3]	381 110.6[−0.3]	413 185.4[−0.7]	
$(n+3)p[1/2]_1$	1/2	311 254.7[0.0]	346 940.6[0.2]	380 804.8[−0.1]	412 969.4[−0.4]	
$(n+2)d[1/2]_0$	1/2		346 923[0.5]			
$(n+3)p[5/2]_2$	5/2	310 311.5[−0.8]	345 956.4[0.3]	379 786.6[0.6]	411 923.6[0.5]	
$(n+3)p[1/2]_1$	3/2	309 062.9[0.0]	344 777.2[0.7]	378 671.4[0.1]	410 868.7[0.5]	
		$n = 50$	$n = 51$	$n = 52$	$n = 53$	
$(n+4)s[3/2]_1$	1/2	30 642[0.3]	81 723.6[−0.7]	129 887.2[−1.2]		
$(n+4)s[3/2]_1$[a]	3/2	27 309.1[−0.1]	78 403.1[−0.3]	126 577.3[−0.6]		
$(n+2)d[3/2]_1$	3/2	17 461.6[1.3]	69 227.2[1.1]	118 024.5[1.3]	164 075.5[0.8]	
$(n+2)d[3/2]_1$	1/2	16 290.9[0.4]	68 050.5[0.4]	116 841.4[0.4]	162 886.9[0.9]	
$(n+2)d[1/2]_1$	1/2	1768[−0.9]	54 483.5[−0.8]	104 156.5[−1.1]	151 017[−1.6]	
$(n+2)d[1/2]_1$	3/2	0.0[0.0]	52 684.7[0.1]	102 328.5[−0.1]	149 161.5[0.1]	
$(n+2)d[1/2]_0$	1/2	−1344[−0.6]	51 410.4[0.0]	101 118.7[0.1]	148 011.4[0.2]	

[a]The assignment of the $[K]_J$ quantum numbers is ambiguous.

in one or two transitions in overview scans, and their positions are indicated with one digit less (their absolute accuracy is about 2 MHz). A few transitions involving np states are split and shifted by small residual electric fields, which mix these states with energetically close-lying $(n-1)d$ states (see the earlier discussion and Figs. 5 and 6). Such cases are marked in Table V and discussed later.

The energy level structures of the odd- and even-parity states determined experimentally are presented in Figs. 7–9, where they are compared with the calculated structures (see below). The $nd[3/2]_1$ states are well separated from the other Rydberg states (see Fig. 7). Therefore the spectra with $nd[3/2]_1(F)$ as initial state are ideally suited to assign the hyperfine structures of the observed transitions and to extract the hyperfine structure of the ion using MQDT calculations. The assignments of the Racah-type $n\ell\,[K]_J$ quantum numbers of the Rydberg levels of ^{129}Xe and ^{131}Xe presented in Tables IV and V are based on the correlation diagrams, calculated by MQDT and depicted in Figs. 10–13, between hyperfine levels of low-n states ($n \approx 30$ for $\ell < 3$), for which the hyperfine splitting is smaller than the separation between the individual $n\ell\,[K]_J$ levels, and $n \approx 60$. For a few hyperfine levels, the assignment of the $[K]_J$ quantum numbers is ambiguous because of avoided crossings; these cases are marked in Tables IV and V. An example is the avoided crossing between the $F = 3/2$ hyperfine levels of the $ns[3/2]_1$ and $ns[3/2]_2$ states of ^{129}Xe around $n \approx 40$ (see the thick dashed lines in Fig. 11). The assignment of the observed hyperfine levels to $ns[3/2]_1$ is based on the assumption that states with predominantly $J = 1$ character are excited from the $6p[1/2]_0(F = I)$ intermediate state by the second laser. Other examples are the avoided crossings between the $F = 3/2$ hyperfine levels of the $np[5/2]_2$ and $np[3/2]_1$ states of ^{129}Xe (thick dashed lines) and between the $F = 5/2$ hyperfine levels of the $np[5/2]_3$ and $np[3/2]_2$ states of ^{129}Xe (thin dash-dotted lines) around $n \approx 45$ (see Fig. 12). In the latter case, the assignment is based on the selection rules for the Stark mixing with the neighboring $(n-1)d[1/2]_1(3/2)$ state (see the subsequent discussion). All assignments are supported by the mixing coefficients A_α determined in the MQDT calculations. For some of the strongly mixed nf hyperfine states, only the K value of the Racah-type $n\ell\,[K]_J$ quantum numbers could be assigned based on the correlation to low-n states ($n \approx 20$) (see Fig. 13).

TABLE V. Rydberg states of ^{131}Xe observed by millimeter-wave spectroscopy. The energies/h (megahertz) are relative to the position of the $52d[1/2]_1(5/2)$ level. The differences between observed and calculated energies $(E_o - E_c)/h$ (megahertz) are given in brackets. The position of the $52d[1/2]_1(5/2)$ level of ^{131}Xe above the $^1S_0$ ($F = 3/2$) ground state is 97 788.960(11) cm^{-1}.

$n\ell\,[K]_J$	F					
		$n = 57$	$n = 58$	$n = 59$	$n = 60$	$n = 61$
$nf[7/2]_3$[a]	7/2			398 976.0[−0.2]	430 258[0.3]	460 013[0.9]
$nf[7/2]_J$[a]	5/2		365 911[0.3]	398 830.0[0.0]	430 117.3[0.2]	459 877.5[0.0]
$nf[7/2]_4$[a]	7/2			398 780.6[0.1]	430 070[0.2]	459 832[0.2]
$nf[7/2]_3$	3/2		365 662.7[0.0]	398 592.4[0.1]	429 889.0[0.1]	459 658.4[−0.1]
$nf[7/2]_J$[a]	5/2		365 583.1[1.0]	398 516.2[0.4]	429 817[0.6]	459 589[0.6]
$nf[5/2]_2$	1/2	330 694.6[0.2]	365 386[−0.4]	398 329.0[−0.4]	429 638.1[−0.1]	459 419[−0.2]
$nf[5/2]_2$[a]	3/2	330 573.3[0.4]	365 273.1[0.3]	398 222.6[0.2]	429 538.2[0.4]	459 325[0.0]
$nf[3/2]_2$[a]	1/2	330 321[−0.9]		398 004.5[−0.5]	429 333.9[−0.6]	459 133[−1.4]
$nf[5/2]_J$[a]	5/2	329 481.4[0.9]	364 148.4[0.5]	397 067.0[0.2]	428 354.0[1.0]	458 114[0.6]
$nf[5/2]_2$[a]	7/2	329 458.6[0.1]	364 129[0.6]	397 050[0.5]	428 338.5[0.8]	458 099[0.1]
$nf[5/2]_3$[a]	3/2	329 437.4[−0.1]	364 103.7[−0.1]	397 021.0[−0.9]	428 308.0[0.0]	458 067[−1.0]
$nf[5/2]_J$[a]	5/2	329 424.1[−0.8]		397 014.1[0.0]	428 301.7[−0.2]	
$nf[5/2]_3$[a]	7/2	329 417.3[0.0]	364 087[−1.2]	397 010[0.4]	428 299[0.2]	458 061[−0.1]
$nf[3/2]_2$	3/2	329 231.3[0.4]	363 922.2[0.8]	396 861.6[0.4]	428 166.8[0.7]	457 943.1[0.4]
$nf[3/2]_1$[a]	1/2	329 177[0.4]	363 872[0.0]	396 815[−0.6]	428 124.5[0.2]	457 905[0.3]
$nf[3/2]_2$	5/2	328 622.5[−0.2]	363 314.5[−0.2]	396 255.1[−0.4]	427 561.2[0.0]	457 338[−0.1]
$nf[3/2]_1$	3/2	328 548.3[−0.5]	363 247.1[0.4]	396 194[0.5]	427 503[−0.1]	
$nf[9/2]_4$	7/2	328 541.2[0.6]	363 231[0.9]	396 171[0.4]	427 475.8[0.8]	457 252[0.6]
$nf[9/2]_4$	5/2	328 235[0.8]	362 931[0.9]	395 877[1.2]	427 187[1.3]	
$nf[9/2]_5$	7/2	328 215[−0.5]	362 914[0.0]	395 863[0.6]	427 177[0.2]	456 963[0.1]
$nf[3/2]_2$	7/2		362 860[0.2]	395 810[0.7]	427 124[0.0]	456 909[−0.1]
$nf[3/2]_1$	5/2	328 057[−0.5]	362 768[0.0]	395 725.5[−0.3]	427 048[0.1]	456 840[0.0]
$(n+3)p[1/2]_0$	3/2			384 861[0.0]		447 194[0.7]
$(n+3)p[3/2]_2$	7/2		349 655.8[−0.4]	383 389.3[−1.3]	415 436.5[−2.2]	445 913[2.6]
$(n+3)p[3/2]_2$	5/2		349 411.3[−0.4]	383 157[−1.2]	415 216.3[−1.2]	445 699[−1.3]
$(n+2)d[1/2]_1$	3/2	312 756[b][5.9]	348 311[b][5.6]	382 054[b][5.5]	414 108[b][7.1]	
$(n+3)p[3/2]_2$	3/2	312 746[b][−2.3]	348 286[b][−2.0]	382 020[b][−0.9]	414 066[b][−1.1]	
$(n+3)p[3/2]_1$	5/2	312 672.9[−0.6]	348 244.0[−1.0]	382 009[b][−0.6]	414 084[b][−2.2]	
$(n+3)p[5/2]_2$[a]	7/2	312 201.1[−1.1]	347 845.2[−0.1]	381 674.7[0.0]	413 811.4[0.4]	
$(n+3)p[3/2]_2$	1/2	312 169.7[1.3]	347 711.8[1.5]	381 448.3[2.8]	413 498[b][3.4]	
$(n+2)d[1/2]_1$	1/2	312 078[−0.8]	347 638.0[−1.4]	381 388.1[−2.6]	413 450[b][−3.3]	
$(n+3)p[3/2]_1$	3/2	311 719.2[−0.1]	347 276.2[−0.1]	381 024.4[−0.4]	413 085.6[−0.2]	
$(n+3)p[3/2]_1$	1/2	311 471.9[−0.1]	347 035.4[−0.2]	380 789.9[−0.2]	412 855.9[−0.3]	
$(n+3)p[5/2]_3$[a]	7/2	311 368.0[0.2]	346 971.1[0.0]	380 762.9[0.1]	412 864.0[0.3]	
$(n+3)p[5/2]_3$[a]	5/2	310 830[−0.6]	346 461.4[−0.2]	380 283.0[−0.3]	412 415.2[0.1]	
$(n+3)p[5/2]_2$[a]	5/2	310 606.3[−0.3]	346 226.8[−0.6]	380 032.1[−0.1]	412 142.7[−0.3]	
$(n+3)p[5/2]_3$	3/2	310 391.2[−0.1]	345 999[0.2]	379 793.9[−0.6]	411 898.7[−1.1]	
$(n+3)p[1/2]_1$	5/2	309 960.7[0.0]	345 658.2[0.3]	379 535.8[0.4]	411 714.4[−0.1]	
$(n+3)p[5/2]_2$	3/2	309 945.6[0.7]	345 591.1[−0.6]	379 423.1[0.1]	411 562.0[0.6]	
$(n+3)p[5/2]_2$	1/2	309 615.0[−1.0]	345 260.0[−0.1]	379 089.9[−0.4]	411 228.2[0.5]	
$(n+3)p[1/2]_1$	3/2	308 894[0.8]	344 604[0.1]	378 496.5[0.4]	410 690.2[0.0]	
$(n+3)p[1/2]_1$	1/2	308 391[0.3]	344 108[0.0]	378 007[0.6]	410 206[−0.3]	
		$n = 50$	$n = 51$	$n = 52$	$n = 53$	
$(n+4)s[3/2]_1$	5/2	29 149.2[0.0]	80 234.8[0.4]	128 402.4[1.2]		
$(n+4)s[3/2]_1$	3/2	27 440.8[0.4]	78 524.9[0.3]	126 690.8[0.4]		
$(n+4)s[3/2]_1$	1/2	26 802.2[−0.1]	77 884.5[−0.4]	126 049.0[−0.4]		
$(n+2)d[3/2]_1$	1/2	16 962.6[−0.5]	68 719.7[−0.2]	117 507.8[0.1]	163 549.2[0.0]	
$(n+2)d[3/2]_1$	3/2	16 691.1[0.0]	68 450.4[0.6]	117 240.4[0.8]	163 284.0[0.7]	
$(n+2)d[3/2]_1$	5/2	16 178.6[−0.1]	67 939.2[0.5]	116 730.9[1.0]	162 776.1[0.9]	
$(n+2)d[1/2]_1$	3/2		53 101.7[0.1]	102 760.5[−0.4]		
$(n+2)d[1/2]_1$	5/2	0.0[0.2]	52 686.8[0.8]	102 331.6[1.0]	149 164.8[1.2]	
$(n+2)d[1/2]_1$	1/2		52 426.0[0.2]	102 081.7[0.0]		

[a]The assignment of the $[K]_J$ quantum numbers is ambiguous.

[b]Found to be strongly perturbed by the Stark effect caused by the stray field.

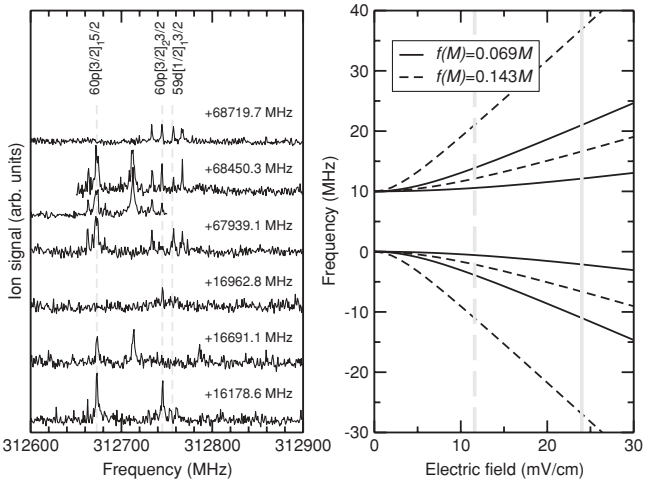

FIG. 6. (left) Millimeter-wave overview spectra of transitions from $nd[3/2]_1(F)$ ($n = 52, 53$) hyperfine levels to $60p[K]_J(F)$ Rydberg states of ^{131}Xe. The spectra are shifted by the frequencies corresponding to the positions of the initial hyperfine levels relative to the $52d[1/2]_1(5/2)$ level (cf. Table V). For the traces shifted by +68 450.3 MHz, the overlap region of two consecutive scans can be compared. The intense lines appearing near the position 312 713 MHz are the transitions to the $60p[5/2]_3(7/2)$ state originating from the $52d[3/2]_1(5/2)$ or $53d[3/2]_1(5/2)$ state, respectively. (right) The Stark effect of the $60p[3/2]_2(3/2)$ and $59d[1/2]_1(3/2)$ Rydberg states has been calculated assuming a field-free state separation of 10 MHz and two different values of $f(M)$ using Eq. (28). The vertical gray lines indicate for each value of $f(M)$ the estimated stray field corresponding to the scans shown in the upper half of the left panel. The scans in the lower half of the left panel were recorded under conditions with very small stray fields so that only transitions to p states were observed.

The MQDT analysis of the hyperfine structure requires complete sets of MQDT parameters for the even- (p, f) and odd-parity (s, d) states. As a primary data source to determine these parameters, the compilation by Saloman

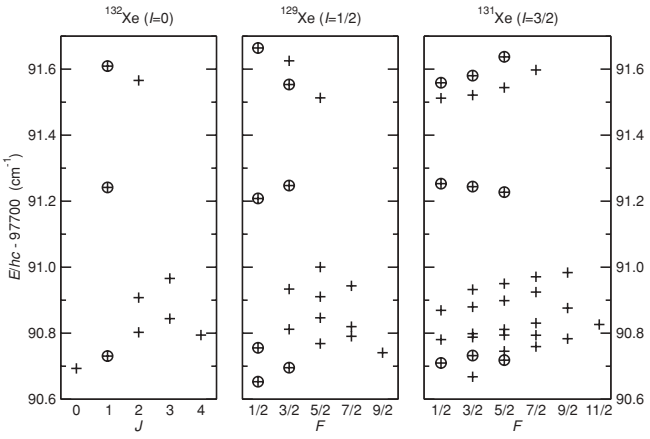

FIG. 7. Calculated (crosses) and observed (circles) positions of the fine and hyperfine levels of the 53d and 55s Rydberg states of ^{132}Xe, ^{129}Xe, and ^{131}Xe. The sequence of the Rydberg levels of ^{132}Xe with increasing energy is $nd[1/2]_0$, $nd[1/2]_1$, $nd[7/2]_4$, $nd[3/2]_2$, $nd[7/2]_3$, $nd[5/2]_2$, $nd[5/2]_3$, $nd[3/2]_1$, $(n+2)s[3/2]_2$, and $(n+2)s[3/2]_1$.

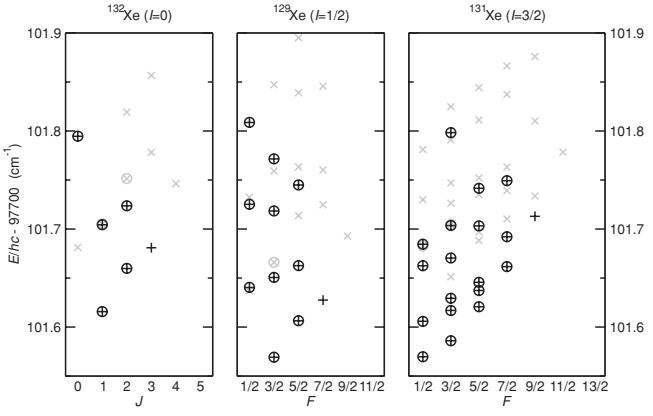

FIG. 8. Calculated (crosses) and observed (circles) positions of the fine and hyperfine levels of the 62p Rydberg states of ^{132}Xe, ^{129}Xe, and ^{131}Xe. The sequence of the Rydberg levels of ^{132}Xe with increasing energy is $np[1/2]_1$, $np[5/2]_2$, $np[5/2]_3$, $np[3/2]_1$, $np[3/2]_2$, and $np[1/2]_0$. Gray crosses indicate the calculated fine and hyperfine levels of the 61d Rydberg states (see Fig. 7), whereas gray circles indicate the observed ones.

[49] has been used. This reference contains the term values of all known Rydberg states with $n \leqslant 20$ for a natural isotope mix. Only a few isotope-selective measurements have been reported, notably the interferometric measurements on ^{136}Xe by Humphreys and Paul [15] and the VUV reference measurement by Brandi *et al.* [48]. Because the isotope shift between the mean level positions of a natural mix and the ^{132}Xe isotope is small (0.002–0.003 cm^{-1} [48]), that is, smaller than the accuracy of most of the earlier experiments and also smaller than the accuracy of the MQDT calculations at low energies, the mean values of the natural mix can be used for the ^{132}Xe isotope. In the following cases, different values than those listed in Ref. [49] have been used: (1) The term values of L'Huillier *et al.* [36] have been found to need a correction of -0.7 cm^{-1}, and the corrected values have been used; (2) the

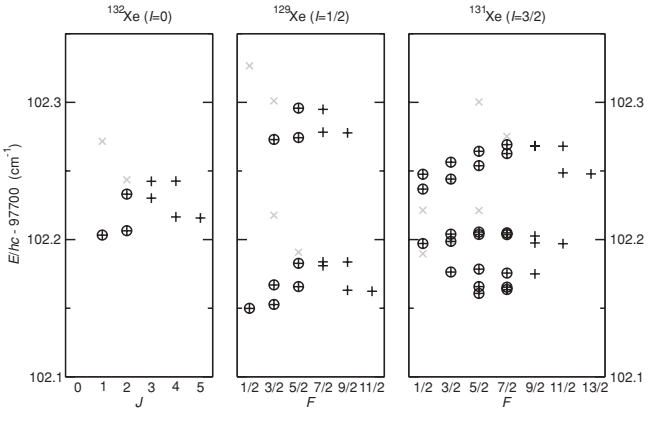

FIG. 9. Calculated (crosses) and observed (circles) positions of the fine and hyperfine levels of the 59f Rydberg states of ^{132}Xe, ^{129}Xe, and ^{131}Xe. The sequence of the Rydberg levels of ^{132}Xe with increasing energy is $nf[3/2]_1$, $nf[3/2]_2$, $nf[9/2]_5$, $nf[9/2]_4$, $nf[5/2]_3$, $nf[5/2]_2$, $nf[7/2]_4$, and $nf[7/2]_3$. Gray crosses indicate the calculated fine and hyperfine levels of the 63s Rydberg states (see Fig. 7).

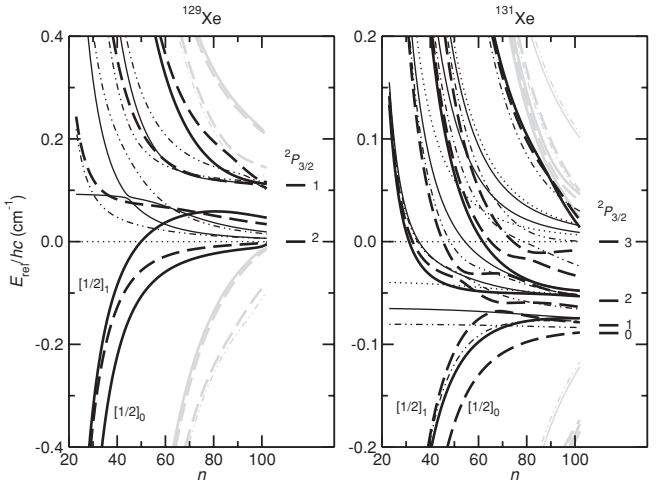

FIG. 10. Calculated hyperfine structure of high-nd Rydberg states relative to the hyperfine level with the highest F value ($F = 9/2$ level for ^{129}Xe and $F = 11/2$ level for ^{131}Xe) belonging to the $nd[7/2]_4$ Rydberg series. The calculated levels with $F = 1/2$ are connected by thick lines, those with $F = 3/2$ by thick dashed lines, those with $F = 5/2$ by thin dash-dotted lines, those with $F = 7/2$ by thin solid lines, and those with $F \geqslant 9/2$ by thin dotted lines. The adjacent $(n + 1)s$ and $(n + 2)s$ Rydberg states are marked with gray lines. On the right-hand side of each panel, the derived hyperfine structure of the cation is shown, labeled with the values of F^+. The number of hyperfine series (and their F values) converging to each ion level can be found in Table II.

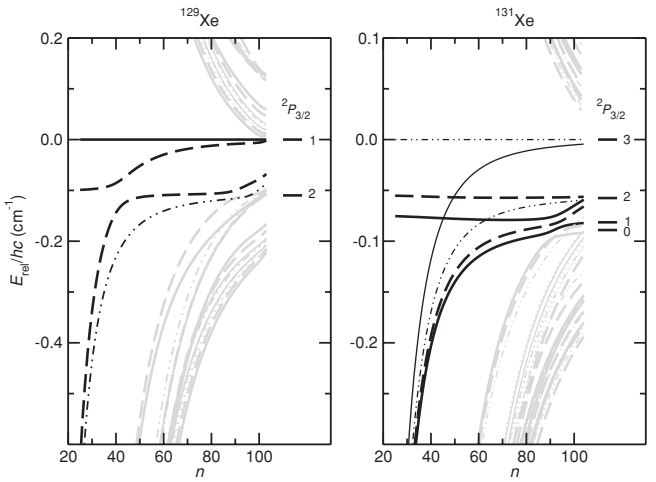

FIG. 11. Calculated hyperfine structure of high-ns Rydberg states relative to the highest hyperfine level ($F = 1/2$ for ^{129}Xe and $F = 5/2$ for ^{131}Xe) of the $ns[3/2]_1$ state. The calculated levels with $F = 1/2$ are connected by thick lines, those with $F = 3/2$ by thick dashed lines, those with $F = 5/2$ by thin dash-dotted lines, those with $F = 7/2$ by thin solid lines, and those with $F \geqslant 9/2$ (d states only) by thin dotted lines. The adjacent $(n - 2)d$ and $(n - 1)d$ Rydberg states are marked with gray lines. The hyperfine levels of the ns states mix with $(n - 2)d$ states above $n = 80$ and with $(n - 1)d$ states above $n = 100$ (for ^{129}Xe). Note the avoided crossing between the $F = 3/2$ hyperfine levels of the $ns[3/2]_1$ and $ns[3/2]_2$ Rydberg states of ^{129}Xe around $n \approx 40$. On the right-hand side of each panel, the derived hyperfine structure of the cation is shown, labeled with the values of F^+.

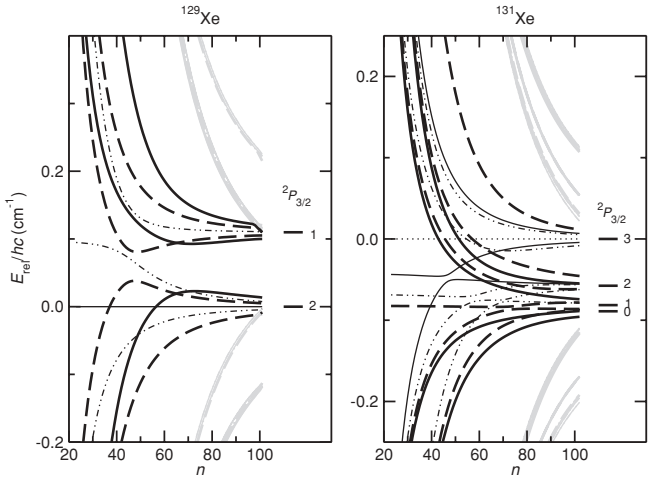

FIG. 12. Calculated hyperfine structure of high-np Rydberg states relative to the hyperfine level with the highest F value ($F = 7/2$ level for ^{129}Xe and $F = 9/2$ level for ^{131}Xe) belonging to the $np[5/2]_3$ Rydberg series. The calculated levels with $F = 1/2$ are connected by thick lines, those with $F = 3/2$ by thick dashed lines, those with $F = 5/2$ by thin dash-dotted lines, those with $F = 7/2$ by thin solid lines, and those with $F = 9/2$ by thin dotted lines. Gray lines indicate the hyperfine levels of the $(n - 3)f$ and $(n - 2)f$ Rydberg states; p-f mixing can be studied in the region where the f states approach the p states, that is, above $n = 90$ for ^{129}Xe and $n > 100$ for ^{131}Xe. On the right-hand side of each panel, the derived hyperfine structure of the cation is shown, labeled with the values of F^+.

values of Refs. [41,44] for the $nf'[5/2]_2$ autoionizing Rydberg series have been adopted, instead of the values of Ref. [11]; and (3) the resonance positions given in Refs. [39,45] have been used for the $nd'[3/2]_1$ autoionizing Rydberg series. For

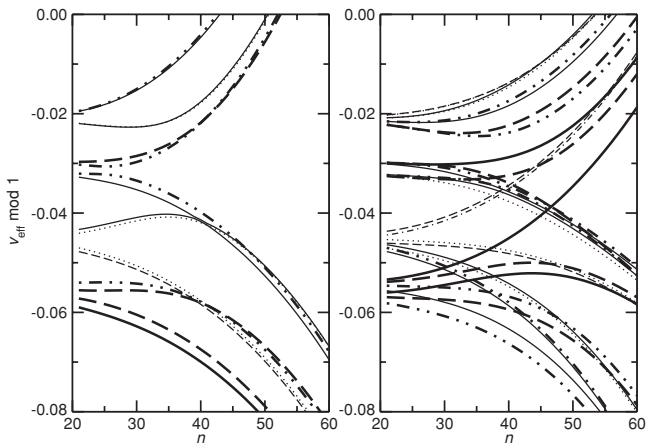

FIG. 13. Calculated hyperfine structure of nf Rydberg states of (left)^{129}Xe and (right) ^{131}Xe, expressed as $\nu_{3/2} - n$ (with $\nu_{3/2}$ defined relative to the center of gravity of the hyperfine structure of the $^2P_{3/2}$ state). The calculated levels with $F = 1/2$ are connected by thick lines, those with $F = 3/2$ by thick dashed lines, those with $F = 5/2$ by thick dash-dotted lines, those with $F = 7/2$ by thin solid lines, those with $F = 9/2$ by thin dotted lines, those with $F = 11/2$ with thin dashed lines, and that with $F = 13/2$ with a thin dash-dotted line. At low n, the typical pattern of Racah-type coupling (with the sequence $nf[3/2]_{1,2}, nf[9/2]_{5,4}, nf[5/2]_{3,2}, nf[7/2]_{4,3}$) is observed.

the terms missing in Ref. [49], the values from the references given in Table I have been used. The energies of the states observed in this study relative to the $(5p)^6\ ^1S_0$ ground state have been obtained by combining the present results with the laser spectroscopic data of the $nf[3/2]_1$ ($n \leqslant 73$) series [29] and the high-resolution data in Refs. [15,48], that is, the values on which the currently adopted ionization energy [48,49] is based.

The autoionizing states between the $^2P_{3/2}$ and $^2P_{1/2}$ ionization limits (ns' levels with $n > 7$, np' levels with $n > 6$, nd' levels with $n > 5$, and all nf' levels) were included in the fit by treating them as bound states by neglecting the coupling to the open channels, that is, by setting $\nu_{i_{(F)}} = 0$ for the open channels (where $E > E_{i_{(F)}}$) in Eqs. (6) and (13). The experimental resonance positions were adopted from the results of the line-shape analysis in the literature. The positions of the sharp $ns'[1/2]_1$ resonances (with $33 \leqslant \nu_{1/2} \leqslant 90$) for ^{129}Xe and ^{131}Xe [76] have been included to ensure that the fitted MQDT parameters describe the autoionizing states as well. The $A_{1/2}$ hyperfine coupling constants for ^{129}Xe and ^{131}Xe and the positions of the ionization thresholds $E(^2P_{1/2})$ were fixed to the values reported in Ref. [9]. The quality of the MQDT parameters were checked by simulating the line shapes of the autoionizing Rydberg states using Eqs. (18)–(22) and comparing them to the experimental line shapes [9,50,57].

Because of the large number of parameters and correlations between parameters, some parameters, in particular, the energy dependence of the quantum defects and several Euler angles θ_{jk}, have been either set to zero or constrained to other values, as follows. For the interactions between the LS-coupled eigenchannels $p^5\ell\ ^{2S+1}L_J$, only interactions between channels with (1) $\Delta\ell = \Delta J = 0$, $\Delta L = 0, \pm 1$, and $\Delta S = 0, \pm 1$ or (2) $\Delta\ell = \pm 2$ and $\Delta L = \Delta S = \Delta J = 0$ were considered. Case 1 represents the nonvanishing matrix elements $\langle L'S'J|\sum_i \xi(r_i)\vec{\ell}_i \cdot \vec{s}_i|LSJ\rangle$ of the spin-orbit interaction [74,77]. The mixing of the s and d eigenchannels (or between p and f channels) (case 2) can be understood as an effect of short-range electrostatic interactions, that is, quadrupole and exchange interactions, and occurs between channels with the same values of L and S [78]. For the energy dependence of the eigenchannel quantum defects μ_α^1, the values for the channels differing only in J were constrained to a common value.

The close-coupling channel parameters μ_α and $V_{\bar{\alpha}\alpha}$ (expressed in terms of the generalized Euler angles θ_{jk}) obtained in the fit and the transformation matrix $U_{i\alpha}$ for the $I = 0$ isotopes are listed in Tables VI and VII, together with the designations of the LS-coupled eigenchannels $\bar{\alpha}$ and of the dissociation channels i. The remaining parameters and results of the MQDT analysis are summarized in Table VIII. The differences between observed and calculated positions of the odd- and even-parity levels presented in Tables III–V are about 1 MHz or less, that is, on the order of the experimental accuracy of our millimeter-wave spectroscopic measurements.

V. DISCUSSION

It has already been mentioned that the $\Delta\ell = \pm 1$ selection rule for electric dipole transitions does not strictly hold for the observed millimeter-wave transitions. The occurrence of $f \leftrightarrow s$ transitions (where the $+ \leftrightarrow -$ selection rule for the parity still holds) can be explained by s-d mixing resulting from the nonspherical charge distribution of the ion core. Transitions between $d[1/2]_1$ and s or d Rydberg states (see Fig. 5) are, in addition, forbidden according to the $+ \leftrightarrow -$ parity selection rule. Such transitions can be interpreted either as electric quadrupole transitions (selection rules $\Delta\ell = 0, \pm 2$ and $|J - J'| \leqslant 2 \leqslant J + J'$) occurring at high millimeter-wave power densities or as arising from Stark mixing of the initial or final state with an energetically close-lying state, with ℓ differing by ± 1, induced by a residual electric field. The matrix element describing the coupling between two states with $\Delta\ell = \pm 1$ caused by an electric field $\mathcal{E}$ in the $J^+\ell$ coupling scheme is [30]

$$\begin{aligned}
&\langle(\nu\ell J^+)KJM|\mathcal{E}ez|(\nu'\ell' J^+)K'J'M\rangle \\
&\quad = (-1)^{J+J'+K+K'+l+J^++s-M}[(2J+1) \\
&\qquad \times (2J'+1)(2K+1)(2K'+1)]^{1/2} \\
&\qquad \times \begin{pmatrix} J & 1 & J' \\ -M & 0 & M \end{pmatrix} \begin{Bmatrix} K & J & s \\ J' & K' & 1 \end{Bmatrix} \\
&\qquad \times \begin{Bmatrix} \ell & K & J^+ \\ K' & \ell' & 1 \end{Bmatrix} \langle\nu\ell||r||\nu'\ell'\rangle\, \mathcal{E}e, \qquad (23)
\end{aligned}$$

with

$$\begin{aligned}
\langle\nu\ell||r||\nu'\ell - 1\rangle &= \sqrt{\ell}\langle\nu\ell|r|\nu'\ell - 1\rangle, \\
\langle\nu\ell||r||\nu'\ell + 1\rangle &= -\sqrt{\ell + 1}\langle\nu\ell|r|\nu'\ell + 1\rangle.
\end{aligned}$$

For isotopes with nonzero nuclear spin, the elements of the Stark-effect operator are

$$\begin{aligned}
&\langle(\nu\ell J^+)KJFM|\mathcal{E}ez|(\nu'\ell' J^+)K'J'F'M\rangle \\
&\quad = (-1)^{F+F'+J+J'+K+K'+l+J^++s+I+1-M} \\
&\qquad \times [(2F+1)(2F'+1)(2J+1)(2J'+1) \\
&\qquad \times (2K+1)(2K'+1)]^{1/2} \\
&\qquad \times \begin{pmatrix} F & 1 & F' \\ -M & 0 & M \end{pmatrix} \begin{Bmatrix} J & F & I \\ F' & J' & 1 \end{Bmatrix} \begin{Bmatrix} K & J & s \\ J' & K' & 1 \end{Bmatrix} \\
&\qquad \times \begin{Bmatrix} \ell & K & J^+ \\ K' & \ell' & 1 \end{Bmatrix} \langle\nu\ell||r||\nu'\ell'\rangle\, \mathcal{E}e \\
&\quad \equiv f(M)\,\langle\nu\ell|r|\nu'\ell'\rangle\, \mathcal{E}e. \qquad (24)
\end{aligned}$$

The six-j symbols in Eqs. (23) and (24) imply the selection rules $\Delta F = 0, \pm 1$, $\Delta J = 0, \pm 1$, and $\Delta K = 0, \pm 1$. For nearly degenerate high-n levels ($|\Delta\nu| \ll 1$), the radial integral can be approximated by [79,80]

$$\langle\nu\ell|r|\nu'\ell - 1\rangle \approx \tfrac{3}{2}\nu\nu'[1 - \ell^2/(\nu\nu')]^{1/2}a_0, \qquad (25)$$

where $\nu = n^*$ stands for the effective principal quantum number and a_0 is the Bohr radius. In the first approximation of perturbation theory, the admixture of a state Ψ_2 in a state Ψ_1 is

$$\frac{\langle\Psi_2|\mathcal{E}ez|\Psi_1\rangle}{E_1 - E_2}\Psi_1. \qquad (26)$$

Thus the matrix element of the "forbidden" transition between initial state Ψ_1 and final state Ψ_3 contains a term

$$\frac{\langle\Psi_2|\mathcal{E}ez|\Psi_1\rangle\langle\Psi_3|\mu|\Psi_2\rangle}{E_1 - E_2}, \qquad (27)$$

TABLE VI. MQDT parameters for odd-parity states of xenon.

	1	2	3	4	5
$J = 0$					
$\bar{\alpha}$	$p^5d\ ^3P_0$	$p^5s\ ^3P_0$			
i	$[^2P_{3/2}]\,d_{3/2}$	$[^2P_{1/2}]\,s_{1/2}$			
μ_α^0	0.54310(21)	0.05125(195)			
μ_α^1	−0.3035(92)	−0.3938(64)			
$U_{1\alpha}$	0.9932	−0.1165			
$U_{2\alpha}$	0.1165	0.9932			
θ_{1k}		0.1168(30)			
$J = 1$					
$\bar{\alpha}$	$p^5d\ ^1P_1$	$p^5d\ ^3P_1$	$p^5d\ ^3D_1$	$p^5s\ ^1P_1$	$p^5s\ ^3P_1$
i	$[^2P_{3/2}]\,d_{5/2}$	$[^2P_{3/2}]\,d_{3/2}$	$[^2P_{1/2}]\,d_{3/2}$	$[^2P_{3/2}]\,s_{1/2}$	$[^2P_{1/2}]\,s_{1/2}$
μ_α^0	0.12802(59)	0.54037(29)	0.37839(101)	0.98705(16)	0.04201(27)
μ_α^1	0.0793(222)	−0.3035[a]	0.3560(155)	−0.2651(163)	−0.3938[b]
$U_{1\alpha}$	0.7490	−0.5535	−0.3323	0.1457	0.0331
$U_{2\alpha}$	0.2717	0.7363	−0.6116	0.0275	−0.0961
$U_{3\alpha}$	0.5780	0.3710	0.7181	0.0908	−0.0665
$U_{4\alpha}$	−0.1441	0.0679	0.0000	0.9135	0.3744
$U_{5\alpha}$	0.1019	0.0961	0.0000	−0.3678	0.9193
θ_{1k}		0.0246(12)	0.0	−0.1774(13)	0.0
θ_{2k}			−0.0285(26)	0.0	0.1179(11)
θ_{3k}				0.0	0.0
θ_{4k}					0.2307(37)
$J = 2$					
$\bar{\alpha}$	$p^5d\ ^3P_2$	$p^5d\ ^3D_2$	$p^5d\ ^3F_2$	$p^5d\ ^1D_2$	$p^5s\ ^3P_2$
i	$[^2P_{3/2}]\,d_{5/2}$	$[^2P_{3/2}]\,d_{3/2}$	$[^2P_{1/2}]\,d_{3/2}$	$[^2P_{1/2}]\,d_{5/2}$	$[^2P_{3/2}]\,s_{1/2}$
μ_α^0	0.53373(53)	0.37551(105)	0.49912(107)	0.38706(68)	0.01802(11)
μ_α^1	−0.3035[a]	0.3560[c]	−0.1301(104)	0.1809(181)	−0.3938[b]
$U_{1\alpha}$	0.6526	−0.2107	−0.1848	0.6978	−0.0934
$U_{2\alpha}$	−0.3101	0.7380	−0.4427	0.4016	0.0444
$U_{3\alpha}$	−0.1475	0.2171	0.8614	0.4344	0.0211
$U_{4\alpha}$	0.6604	0.6032	0.1670	−0.4039	−0.0945
$U_{5\alpha}$	0.1417	0.0000	0.0000	0.0000	0.9899
θ_{1k}		−0.0420(25)	0.0	0.0	0.1422(32)
θ_{2k}			0.0149(51)	0.0630(221)	0.0
θ_{3k}				0.0	0.0
θ_{4k}					0.0
$J = 3$					
$\bar{\alpha}$	$p^5d\ ^3D_3$	$p^5d\ ^3F_3$	$p^5d\ ^1F_3$		
i	$[^2P_{3/2}]\,d_{5/2}$	$[^2P_{3/2}]\,d_{3/2}$	$[^2P_{1/2}]\,d_{5/2}$		
μ_α^0	0.37942(97)	0.48994(82)	0.37801(198)		
μ_α^1	0.3560[c]	−0.1301[d]	−0.0779(198)		
$U_{1\alpha}$	0.8494	−0.0599	0.5244		
$U_{2\alpha}$	−0.2923	0.7739	0.5619		
$U_{3\alpha}$	0.4395	0.6305	−0.6398		
θ_{1k}		−0.0471(99)	0.0		
θ_{2k}			0.0946(79)		
$J = 4$					
$\bar{\alpha}$	$p^5d\ ^3F_4$				
i	$[^2P_{3/2}]\,d_{5/2}$				
μ_α^0	0.47993(23)				
μ_α^1	−0.1301[d]				

[a]Constrained to the value of the $d\ ^3P_0$ eigenchannel.
[b]Constrained to the value of the $s\ ^3P_0$ eigenchannel.
[c]Constrained to the value of the $d\ ^3D_1$ eigenchannel.
[d]Constrained to the value of the $d\ ^3F_2$ eigenchannel.

TABLE VII. MQDT parameters for even-parity states of xenon.

	1	2	3	4	5	6
$J = 0$						
$\tilde{\alpha}$	$p^5 p\ ^1S_0$	$p^5 p\ ^3P_0$				
i	$[^2P_{1/2}]\ p_{1/2}$	$[^2P_{3/2}]\ p_{3/2}$				
μ_α^0	0.41217(89)	0.56131(175)				
μ_α^1	−0.4886(206)	−0.4021(153)				
$U_{1\alpha}$	0.3413	0.9400				
$U_{2\alpha}$	0.9400	−0.3413				
θ_{1k}		−0.2672(43)				
$J = 1$						
$\tilde{\alpha}$	$p^5 p\ ^3S_1$	$p^5 p\ ^1P_1$	$p^5 p\ ^3P_1$	$p^5 p\ ^3D_1$	$p^5 f\ ^3D_1$	
i	$[^2P_{1/2}]\ p_{1/2}$	$[^2P_{1/2}]\ p_{3/2}$	$[^2P_{3/2}]\ p_{1/2}$	$[^2P_{3/2}]\ p_{3/2}$	$[^2P_{3/2}]\ f_{5/2}$	
μ_α^0	0.53163(195)	0.63549(69)	0.51197(27)	0.61857(116)	0.05763(10)	
μ_α^1	−0.4723(340)	−0.4877(218)	−0.4021[a]	−0.3964(17)	0.3693(154)	
$U_{1\alpha}$	−0.1883	0.1636	0.2212	0.9422	−0.0338	
$U_{2\alpha}$	0.6785	−0.6662	−0.1289	0.2812	−0.0101	
$U_{3\alpha}$	−0.3867	−0.5875	0.6972	−0.1388	0.0050	
$U_{4\alpha}$	0.5955	0.4293	0.6696	−0.1126	0.0040	
$U_{5\alpha}$	0.0000	0.0000	0.0000	0.0358	0.9994	
θ_{1k}		0.0	0.2078(32)	0.0	0.0	
θ_{2k}			−1.1337(27)	0.0	0.0	
θ_{3k}				−0.2457(31)	0.0	
θ_{4k}					0.0359(28)	
$J = 2$						
$\tilde{\alpha}$	$p^5 p\ ^3P_2$	$p^5 p\ ^1D_2$	$p^5 p\ ^3D_2$	$p^5 f\ ^1D_2$	$p^5 f\ ^3D_2$	$p^5 f\ ^3F_2$
i	$[^2P_{1/2}]\ p_{3/2}$	$[^2P_{3/2}]\ p_{1/2}$	$[^2P_{3/2}]\ p_{3/2}$	$[^2P_{1/2}]\ f_{5/2}$	$[^2P_{3/2}]\ f_{5/2}$	$[^2P_{3/2}]\ f_{7/2}$
μ_α^0	0.49701(21)	0.50998(51)	0.61608(66)	0.05052(13)	0.05849(11)	0.01368(15)
μ_α^1	−0.4021[a]	−0.7647(227)	−0.3964[b]	0.0	0.3693[c]	0.0434(206)
$U_{1\alpha}$	0.3219	−0.5146	0.7947	−0.0044	−0.0011	0.0000
$U_{2\alpha}$	−0.4889	0.6284	0.6050	0.0054	−0.0005	0.0000
$U_{3\alpha}$	0.8108	0.5832	0.0493	0.0050	0.0001	0.0000
$U_{4\alpha}$	0.0000	−0.0050	0.0058	0.5594	0.4885	0.6697
$U_{5\alpha}$	0.0000	−0.0027	0.0077	0.2849	0.6453	−0.7087
$U_{6\alpha}$	0.0000	−0.0065	−0.0075	0.7783	−0.5873	−0.2218
θ_{1k}		0.0	−0.1184(28)	0.0	0.0	0.0
θ_{2k}			0.0812(27)	−0.0086(32)	0.0	0.0
θ_{3k}				0.0	0.0012(39)	0.0
θ_{4k}					−0.0372(30)	0.0
θ_{5k}						−0.0061(27)
$J = 3$						
$\tilde{\alpha}$	$p^5 p\ ^3D_3$	$p^5 f\ ^3D_3$	$p^5 f\ ^1F_3$	$p^5 f\ ^3F_3$	$p^5 f\ ^3G_3$	
i	$[^2P_{3/2}]\ p_{3/2}$	$[^2P_{1/2}]\ f_{5/2}$	$[^2P_{1/2}]\ f_{7/2}$	$[^2P_{3/2}]\ f_{5/2}$	$[^2P_{3/2}]\ f_{7/2}$	
μ_α^0	0.53968(5)	0.05538(22)	0.01714(5)	0.01764(17)	0.03657(5)	
μ_α^1	−0.3964[b]	0.3693[c]	0.2277(516)	0.0434[d]	0.2188(354)	
$U_{1\alpha}$	0.9993	0.0375	0.0000	−0.0003	0.0000	
$U_{2\alpha}$	0.0040	−0.1043	0.4465	0.2038	0.8650	
$U_{3\alpha}$	−0.0276	0.7418	−0.3554	0.5497	0.1435	
$U_{4\alpha}$	0.0071	−0.1844	0.5167	0.7019	−0.4543	
$U_{5\alpha}$	−0.0239	0.6352	0.6383	−0.4046	−0.1574	
θ_{1k}		−0.0375(31)	0.0	0.0	0.0	
θ_{2k}			0.0	0.0084(31)	0.0	
θ_{3k}				0.0413(98)	0.0	
θ_{4k}					−0.0358(42)	
$J = 4$						
$\tilde{\alpha}$	$p^5 f\ ^3F_4$	$p^5 f\ ^1G_4$	$p^5 f\ ^3G_4$			
i	$[^2P_{1/2}]\ f_{7/2}$	$[^2P_{3/2}]\ f_{5/2}$	$[^2P_{3/2}]\ f_{7/2}$			
μ_α^0	0.01429(11)	0.04508(15)	0.04681(20)			
μ_α^1	0.0434[d]	0.2607(501)	0.2188[e]			

TABLE VII. (*Continued.*)

	1	2	3	4	5	6
$U_{1\alpha}$	0.4923	−0.5735	0.6548			
$U_{2\alpha}$	−0.1977	0.6590	0.7257			
$U_{3\alpha}$	0.8477	0.4867	−0.2110			
θ_{1k}		0.0	−0.0119(43)			
θ_{2k}			0.0059(83)			
$J = 5$						
$\bar{\alpha}$	$p^5 f\ ^3G_5$					
i	$[^2P_{3/2}]\ f_{7/2}$					
μ_α^0	0.04655(5)					
μ_α^1	0.2188[e]					

[a]Constrained to the value of the $p\ ^3P_0$ eigenchannel.
[b]Constrained to the value of the $p\ ^3D_1$ eigenchannel.
[c]Constrained to the value of the $f\ ^3D_1$ eigenchannel.
[d]Constrained to the value of the $f\ ^3F_2$ eigenchannel.
[e]Constrained to the value of the $f\ ^3G_3$ eigenchannel.

which is not zero if transitions from the "intermediate" state Ψ_2 to the initial state Ψ_1 and final state Ψ_3 are allowed [81]. Significant Stark mixing occurs when the matrix element is of the same order of magnitude as the energy difference between the states $\Delta E \approx 2hcR_M\Delta\nu/\nu^3$, that is, at electric fields $\mathcal{E} \sim \Delta\nu/\nu^5$ (in atomic units of the electric field[1]). As a consequence of this n^{-5} scaling law, such mixing occurs easily for very high n Rydberg states. For instance, transitions from d states to nd or ns Rydberg states with $n > 150$ have been observed in millimeter-wave spectra of krypton induced by electric fields as low as 2.5 mV/cm [67]. Because the $np[3/2]_1$ and $(n-1)d[1/2]_1$ Rydberg states are energetically very close ($\Delta\nu_{3/2} = 0.0007$), $\Delta\nu/\nu^5$ corresponds to an electric field of 10 mV/cm for $n = 55$ or 4.8 mV/cm for $n = 63$, and observable mixing arises at even smaller stray fields.

The field-induced shift of the energies of two near-degenerate levels (separated by $\Delta\nu/\nu^3$) with $\Delta\ell = \pm 1$ can be estimated from the relation (expressed in atomic units; see Footnote 1)

$$|\Delta E| = \left[\left|\langle \nu\ell FM|\mathcal{E}ez|\nu'\ell'F'M\rangle\right|^2 + \left(\frac{\Delta\nu}{2\nu^3}\right)^2\right]^{1/2} - \frac{\Delta\nu}{2\nu^3} \approx \frac{\Delta\nu}{2\nu^3}\left\{\left[\left(\frac{3f(M)\mathcal{E}\nu^5}{\Delta\nu}\right)^2 + 1\right]^{1/2} - 1\right\}. \quad (28)$$

For weak fields or $\mathcal{E}\nu^5/\Delta\nu \ll 1$, a quadratic Stark shift

$$|\Delta E| = \frac{\Delta\nu}{\nu^3}\left(\frac{3f(M)\mathcal{E}\nu^5}{2\Delta\nu}\right)^2$$
$$|\Delta E/h| = 5.60\times 10^{-13}\,\text{kHz}\,[f(M)(\mathcal{E}/\text{mV cm}^{-1})]^2\frac{\nu^7}{\Delta\nu} \quad (29)$$

results, whereas in the case $\mathcal{E}\nu^5/\Delta\nu \gg 1$, a linear Stark shift

$$|\Delta E = \tfrac{3}{2}|f(M)\mathcal{E}|\nu^2$$
$$|\Delta E/h| = 1.92\,\text{kHz}\,|f(M)(\mathcal{E}/\text{mV cm}^{-1})|\nu^2 \quad (30)$$

is obtained with $|f(M)| < 0.5$ for interacting p and d states. Numerical evaluation of Eq. (28) yields, for a residual field of

[1]Atomic units: energy $E_h = \hbar^2/m_e a_0^2 = 2R_\infty hc = 4.3597\times 10^{-18}$ J; electric field $E_h/ea_0 = 5.1422\times 10^{12}$ mV/cm.

TABLE VIII. The fine and hyperfine structure of the ^2P ground state of Xe^+ as determined from the MQDT analysis.

	^{129}Xe	^{131}Xe	^{132}Xe
R_M (cm^{-1})	109 736.8487	109 736.8558	109 736.8593
$E(^2P_{3/2})/hc$ (cm^{-1})	97 833.778[a]	97 833.783[a]	97 833.790[a]
$E(^2P_{1/2})/hc$ (cm^{-1})	108 370.705[b,c]	108 370.711[b,c]	108 370.714[b,c]
$(E(^2P_{3/2}) - E_{\text{ref}})/hc$ [d] (cm^{-1})	44.839 718(29)	44.822 516(28)	44.817 421(31)
$A_{3/2}$ (cm^{-1})	−0.054 9265(52)	0.016 2829(21)	
$B_{3/2}$ (cm^{-1})		0.008 6887(82)	
$A_{1/2}$ (cm^{-1})	−0.4071[b]	0.1206[b]	
σ_{mmwave} (MHz)	0.6	0.7	0.5

[a]Fixed to the value given in Ref. [48] (with uncertainty of 0.011 cm^{-1}).
[b]Fixed to the value given in Ref. [9].
[c]The uncertainty in the VUV calibration is 0.016 cm^{-1}.
[d]The reference level E_{ref} is $52d[1/2]_1$ (or its $F = 3/2$ or $F = 5/2$ hyperfine level for ^{129}Xe and ^{131}Xe, respectively).

5 mV/cm, a Stark shift of 0.29 MHz for the $M = 1$ levels of the $63p[3/2]_1$ and $62d[1/2]_1$ states of ^{132}Xe [$f(1) = 0.0745$ for purely $J^+\ell$-coupled states]; the magnitude of this shift is less than the frequency accuracy estimated in Sec. II. Thus the presence of a stray electric field is revealed by the observation of the "forbidden" transition to the $nd[1/2]_1$ state rather than by a measurable shift of the transition frequency. The excessive broadening of the $np[3/2]_1 \leftarrow n'd[3/2]_1$ transitions, compared to the "forbidden" $(n-1)d[1/2]_1 \leftarrow n'd[3/2]_1$ transitions and transitions to other np states (see Figs. 2 and 5), can be attributed to power broadening. The same arguments have been used for the assignment of several transitions of ^{129}Xe or ^{131}Xe; for example, the transitions to the $np[3/2]_2(5/2)$ states of ^{129}Xe are broader than the transition to the neighboring $(n-1)d[1/2]_1(3/2)$ states.

In several overview scans for ^{131}Xe recorded without compensation of stray fields, series of four almost equidistant lines separated by about 11 MHz were observed in the region of the $60p[3/2]_2(3/2)$ final state (see Fig. 6). Such a quartet structure can be explained by two almost degenerate (separated by $\Delta E/h \lesssim 10$ MHz) np and $(n-1)d$ levels with $F = 3/2$, split by an electric stray field. If we assume that the interacting state is a pure $59d[1/2]_1(3/2)$ state, for which $f(M) = 0.069M$, the stray field must have been of the order of $\mathcal{E} = 24$ mV/cm according to Eq. (30). The avoided crossings between the $F = 3/2$ series (thick dashed lines) in Fig. 10 indicate an admixture of the $59d[3/2]_2(3/2)$ state, which would lead to a larger value for the Stark effect matrix element [$f(M) = -0.143M$] so that the magnitude of the stray field was probably less than the value calculated previously. In other scans with smaller stray fields, only one line was observed corresponding to the position of the $60p[3/2]_2(3/2)$ state.

Depending on the experimental conditions, the Stark effect also led, in some spectra, to a broadening (and a shift) of the transitions to f levels, which can be mixed with $\ell > 3$ states (see Fig. 4).

The MQDT parameters in Tables VI and VII represent effective parameters which describe the Rydberg states observed in the millimeter-wave experiments with very high accuracy. For low-n Rydberg states ($\nu_{3/2} \leqslant 10$), the agreement between calculated and experimental positions is not as good because solely a linear energy dependence of the quantum defects was included in the fit. In addition, the use of μ quantum defects yields at very low energies unphysical solutions of the MQDT equation corresponding to nonexistant $\ell > 0$ states. An approach which does not give such "spurious" roots and avoids an unconvenient energy dependence of the MQDT parameters has been proposed recently [82]. Nevertheless, for most of the low-n Rydberg levels, the errors in the effective quantum number $\nu_{3/2}$ obtained using our MQDT parameters are much smaller than 0.01, and the calculated hyperfine structure of levels with $\nu_{3/2}$ as low as 4.40 agrees reasonably well with the experimental results (see Table IX).

Even though the MQDT parameters in Tables VI and VII are effective ones, which depend on the selections (constraints) made in the fit, some conclusions on the odd-parity channels can be derived from these parameters. As has been observed for krypton [6], the quantum defects μ_α are almost independent of the J value, and only the Euler angles θ_{jk} which correspond to the s-d interaction [$\theta(d\,^1P_1\text{–}s\,^1P_1) \approx 0.18$ and $\theta(d\,^3P_J\text{–}s\,^3P_J) \approx 0.12$] (see Table X) and to the singlet-triplet interaction ($|\theta| \leqslant 0.3$) are significant. Comparing the results with literature values for $J = 1$, it is found that the absolute values of the Euler angles (or the transformation matrix elements $U_{i\alpha}$) and the energy dependencies of the eigenchannel quantum defects μ_α^1 obtained by Johnson *et al.* [60] from ab initio calculations and adjusted to spectra of the autoionizing Rydberg series are the ones which come closest

TABLE IX. Calculated (MQDT) and observed hyperfine structure of low-n Rydberg states of xenon.

State[a]		$\Delta\nu_{\text{calc}}$ (MHz)	$\Delta\nu_{\text{obs}}$ (MHz)
$8p[1/2]_1$	^{129}Xe 1/2–3/2	2262	2340(3) [35]
(92 153.279 cm^{-1})	^{131}Xe 5/2–3/2	1160	1215(3) [35]
	^{131}Xe 3/2–1/2	596	585(3) [35]
$7d[3/2]_1$	^{129}Xe 3/2–1/2	236	206(11) [53]
(92 714.038 cm^{-1})	^{131}Xe 3/2–1/2	76	75(33) [53]
	^{131}Xe 1/2–5/2	122	115(41) [53]
$5d'[3/2]_1$	^{129}Xe 3/2–1/2	2563	2486(18) [48]
(93 618.24 cm^{-1})	^{131}Xe 1/2–3/2	803	797(23) [48]
	^{131}Xe 3/2–5/2	1242	1200(18) [48]
$8d[1/2]_1$	^{129}Xe 1/2–3/2	894	869(9) [48]
(94 228.006 cm^{-1})	^{131}Xe 5/2–3/2	324	328(19) [48]
	^{131}Xe 3/2–1/2	474	398(14) [48]
$8d[3/2]_1$	^{129}Xe 3/2–1/2	1558	1369(34) [48]
(94 685.470 cm^{-1})	^{131}Xe 1/2–3/2	504	467(20) [48]
	^{131}Xe 3/2–5/2	746	625(30) [48]
$7s'[1/2]_1$	^{129}Xe 1/2–3/2	6314	6822(23) [48]
(95 800.587 cm^{-1})	^{131}Xe 5/2–3/2	3089	3336(9) [48]
	^{131}Xe 3/2–1/2	1922	2063(17) [48]

[a]The experimental level positions of the ^{132}Xe isotope are given.

TABLE X. s-d and singlet-triplet channel interactions in rare gas atoms. The parameters are expressed as absolute values of the generalized Euler angles θ (radian).

	s-d				$^1P_1$-$^3P_1$		
	$^1P_1$	$^3P_0$	$^3P_1$	$^3P_2$	s	d	Note
Ne	0.032	0.0374	0.051		0	0	Ref. [85]
	0.008	0.0374	0.050	0.038	0	0	Ref. [86]
	0.0315		0.0489		0	0	Ref. [87]
Ar	0.02		0.18		0.02	0.0	Ref. [78][a]
	0.042		0.097		0.023	(0.006)	Ref. [60][b]
				0.101			Ref. [88]
Kr	0.485	0.154	0.142	0.128	0.037	0.016	Ref. [6]
	0.495		0.148		0.125	(0.009)	Ref. [60][b]
	(0.0)	0.172	0.102	0.12	0.038	(0.0)	Ref. [73][c]
	(0.018)		0.080		(0.002)	0.042	Ref. [59][d]
Xe	0.177	0.117	0.118	0.142	0.231	0.025	This study
	0.099		0.109		0.245	0.038	Ref. [60][b]
	(0.014)		0.062		0.378	0.043	Ref. [59][d]
		0.1065					Ref. [61]

[a]Ab initio values.
[b]Derived from the $U_{i\alpha}$ matrix based on ab initio values.
[c]Derived from the $U_{i\alpha}$ matrices.
[d]Derived from the $U_{i\alpha}$ matrix.

to the values of this study. A similar observation was made in the millimeter-wave study of Rydberg states of krypton [6]. That study differs from the present one by the fact that more information about the s and d Rydberg states were obtained because p Rydberg states with $J = 1, 2$ were used as initial states for the millimeter-wave transitions, giving access to a broader range of s and d Rydberg states. In addition, an avoided crossing between hyperfine levels of $nd[3/2]_1$ and $(n+2)s[3/2]_J$ was directly observed near $n \approx 70$ and could be exploited to derive accurate s-d channel-mixing parameters; to obtain such information with the same accuracy in xenon, Rydberg states above $n = 80$ would have to be accessed (see Fig. 11). Another range to study the s-d interaction is where the highest $(n-1)s$ hyperfine level meets the lowest nd level; in ^{129}Xe, this range is located around $n = 100$. In Table X, the s-d and singlet-triplet channel-interaction parameters of xenon are compared to those of other rare gases. Values in parentheses are considered to be not significant because other interaction parameters (not included in this table) are much larger. Despite significant differences between the results of different studies, the singlet-triplet interaction parameters show a tendency to increase with increasing nuclear charge. For the s-d interaction, the largest values are obtained for krypton. Considering the MQDT parameters of the even-parity states, it might be noted that most Euler angles are small, except for $J = 1$. To study the interaction between p and f states, it would be necessary to access Rydberg states around $n = 100$ for ^{129}Xe and $n = 120$ for ^{131}Xe.

The hyperfine structures of the $^2P_{3/2}$ state of $^{129}Xe^+$ and $^{131}Xe^+$ determined in this study are summarized in Table VIII and displayed in Fig. 1. The ratio $A(^{129}\mathrm{Xe})/A(^{131}\mathrm{Xe})$ provides a consistency check of the hyperfine constants. The magnetic dipole constant A is proportional to the ratio of the nuclear magnetic moment μ and the nuclear spin quantum number I, thus $A(^{129}\mathrm{Xe})/A(^{131}\mathrm{Xe}) = [\mu(^{129}\mathrm{Xe})I(^{131}\mathrm{Xe})]/[\mu(^{131}\mathrm{Xe})I(^{129}\mathrm{Xe})]$. The ratio of the constants determined in this work, $A(^{129}\mathrm{Xe})/A(^{131}\mathrm{Xe}) = -3.373\,26(75)$ for the $^2P_{3/2}$ state, corresponds well to the value $A(^{129}\mathrm{Xe})/A(^{131}\mathrm{Xe}) = -3.375(12)$ determined for the $^2P_{1/2}$ state [9] and to $A(^{129}\mathrm{Xe})/A(^{131}\mathrm{Xe}) = 3.373\,40(5)$ obtained using the literature values $\mu(^{129}\mathrm{Xe}) = 0.777\,976(8)\,\mu_N$ and $\mu(^{131}\mathrm{Xe}) = 0.691\,862(4)\,\mu_N$ from Refs. [83,84].

ACKNOWLEDGMENTS

We thank Prof. E. R. Grant (University of British Columbia) for useful discussions in the initial phase of the experiments. This work is supported by ETH Zürich (Project No. TH 29/04-3) and the Swiss National Science Foundation (Project No. NF 20020-125030/1).

[1] G. Herzberg and C. Jungen, J. Mol. Spectrosc. **41**, 425 (1972).
[2] F. Merkt and A. Osterwalder, Int. Rev. Phys. Chem. **21**, 385 (2002).
[3] M. Schäfer and F. Merkt, in *Frontiers of Molecular Spectroscopy*, edited by J. Laane (Elsevier, Amsterdam, 2009), p. 35.
[4] A. Osterwalder, A. Wüest, F. Merkt, and C. Jungen, J. Chem. Phys. **121**, 11810 (2004).
[5] H. A. Cruse, C. Jungen, and F. Merkt, Phys. Rev. A **77**, 042502 (2008).
[6] M. Schäfer and F. Merkt, Phys. Rev. A **74**, 062506 (2006).
[7] H. J. Wörner, U. Hollenstein, and F. Merkt, Phys. Rev. A **68**, 032510 (2003).
[8] T. A. Paul, J. Liu, and F. Merkt, Phys. Rev. A **79**, 022505 (2009).
[9] H. J. Wörner, M. Grütter, E. Vliegen, and F. Merkt, Phys. Rev. A **71**, 052504 (2005); **73**, 059904(E) (2006).
[10] C. E. Moore, *Atomic Energy Levels*, Vol. III, National Bureau of Standard (US) Circ. No. 467 (US Government Printing Office, Washington, DC, 1958).
[11] M. Thekaekara and G. H. Dieke, Phys. Rev. **109**, 2029 (1958).
[12] W. L. Faust and M. N. McDermott, Phys. Rev. **123**, 198 (1961).
[13] C. J. Humphreys, E. Paul Jr., R. D. Cowan, and K. L. Andrew, J. Opt. Soc. Am. **57**, 855 (1967).
[14] F. J. Comes, H. G. Sälzer, and G. Schumpe, Z. Naturforsch. **23**a, 137 (1968).
[15] C. J. Humphreys and E. Paul Jr., J. Opt. Soc. Am. **60**, 1302 (1970).
[16] D. A. Jackson and M. C. Coulombe, Proc. R. Soc. London A **327**, 137 (1972).
[17] D. A. Jackson and M. C. Coulombe, Proc. R. Soc. London A **335**, 127 (1973).
[18] W. Fischer, H. Hühnermann, G. Krömer, and H. J. Schäfer, Z. Phys. **270**, 113 (1974).
[19] D. A. Jackson and M.-C. Coulombe, Proc. R. Soc. London A **338**, 277 (1974).
[20] D. A. Jackson, M.-C. Coulombe, and J. Bauche, Proc. R. Soc. London A **343**, 443 (1975).
[21] D. A. Jackson and M.-C. Coulombe, Proc. R. Soc. London A **343**, 453 (1975).
[22] R. D. Rundel, F. B. Dunning, H. C. Goldwire Jr., and R. F. Stebbings, J. Opt. Soc. Am. **65**, 628 (1975).
[23] K. Radler and J. Berkowitz, J. Chem. Phys. **70**, 216 (1979).
[24] J.-P. Grandin and X. Husson, J. Phys. B **14**, 433 (1981).
[25] H. Gerhardt, F. Jeschonnek, W. Makat, E. Matthias, H. Rinneberg, F. Schneider, A. Timmermann, R. Wenz, and P. J. West, Hyperfine Interact. **9**, 175 (1981).
[26] P. Labastie, F. Biraben, and E. Giacobino, J. Phys. B **15**, 2595 (1982).
[27] K. Yoshino and D. E. Freeman, J. Opt. Soc. Am. B **2**, 1268 (1985).
[28] K. D. Bonin, T. J. McIlrath, and K. Yoshino, J. Opt. Soc. Am. B **2**, 1275 (1985).
[29] R. D. Knight and L. G. Wang, J. Opt. Soc. Am. B **2**, 1084 (1985).
[30] R. D. Knight and L. G. Wang, Phys. Rev. A **32**, 896 (1985).
[31] R. D. Knight and L. G. Wang, J. Opt. Soc. Am. B **3**, 1673 (1986).
[32] L. G. Wang and R. D. Knight, Phys. Rev. A **34**, 3902 (1986).
[33] P. R. Blazewicz, J. A. D. Stockdale, J. C. Miller, T. Efthimiopoulos, and C. Fotakis, Phys. Rev. A **35**, 1092 (1987).
[34] W. E. Ernst, T. P. Softley, and R. N. Zare, Phys. Rev. A **37**, 4172 (1988).

[35] H. Geisen, T. Krümpelmann, D. Neuschäfer, and C. Ottinger, Phys. Lett. A **130**, 299 (1988).
[36] A. L'Huillier, L.-A. Lompre, D. Normand, J. Morellec, M. Ferray, J. Lavancier, G. Mainfray, and C. Manus, J. Opt. Soc. Am. B **6**, 1644 (1989).
[37] J. Z. Wu, S. B. Whitfield, C. D. Caldwell, M. O. Krause, P. van der Meulen, and A. Fahlman, Phys. Rev. A **42**, 1350 (1990).
[38] D. Klar, K. Harth, J. Ganz, T. Kraft, M.-W. Ruf, H. Hotop, V. Tsemekhman, K. Tsemekhman, and M. Y. Amusia, Z. Phys. D **23**, 101 (1992).
[39] K. Maeda, K. Ueda, and K. Ito, J. Phys. B **26**, 1541 (1993).
[40] S. M. Koeckhoven, W. J. Buma, and C. A. de Lange, Phys. Rev. A **49**, 3322 (1994).
[41] S. M. Koeckhoven, W. J. Buma, and C. A. de Lange, Phys. Rev. A **51**, 1097 (1995).
[42] R. Kau, D. Klar, S. Schohl, S. Baier, and H. Hotop, Z. Phys. D **36**, 23 (1996).
[43] M. Ahmed, M. A. Baig, and B. Suleman, J. Phys. B **31**, 4017 (1998).
[44] M. Gisselbrecht, A. Marquette, and M. Meyer, J. Phys. B **31**, L977 (1998).
[45] A. Kortyna, M. R. Darrach, P.-T. Howe, and A. Chutjian, J. Opt. Soc. Am. B **17**, 1934 (2000).
[46] G. D'Amico, G. Pesce, and A. Sasso, Hyperfine Interact. **127**, 121 (2000).
[47] M. Hanif, M. Aslam, R. Ali, A. Nadeem, M. Riaz, S. A. Bhatti, and M. A. Baig, J. Phys. B **33**, 4647 (2000).
[48] F. Brandi, I. Velchev, W. Hogervorst, and W. Ubachs, Phys. Rev. A **64**, 032505 (2001).
[49] E. B. Saloman, J. Phys. Chem. Ref. Data **33**, 765 (2004).
[50] M. Hanif, M. Aslam, R. Ali, S. A. Bhatti, M. A. Baig, D. Klar, M.-W. Ruf, I. D. Petrov, V. L. Sukhorukov, and H. Hotop, J. Phys. B **37**, 1987 (2004).
[51] S. Aloïse, P. O'Keeffe, D. Cubaynes, M. Meyer, and A. N. Grum-Grzhimailo, Phys. Rev. Lett. **94**, 223002 (2005).
[52] T. Peters, T. Halfmann, U. Even, A. Wünnenberg, I. D. Petrov, V. L. Sukhorukov, and H. Hotop, J. Phys. B **38**, S51 (2005).
[53] T. A. Paul and F. Merkt, J. Phys. B **38**, 4145 (2005).
[54] R. Seiler, T. Paul, M. Andrist, and F. Merkt, Rev. Sci. Instrum. **76**, 103103 (2005).
[55] M. Hanif, M. Aslam, M. Riaz, S. A. Bhatti, and M. A. Baig, J. Phys. B **38**, S65 (2005).
[56] I. D. Petrov, T. Peters, T. Halfmann, S. Aloïse, P. O'Keeffe, M. Meyer, V. L. Sukhorukov, and H. Hotop, Eur. Phys. J. D **40**, 181 (2006).
[57] M. A. Baig, M. Hanif, M. Aslam, and S. A. Bhatti, J. Phys. B **39**, 4221 (2006).
[58] K. T. Lu, Phys. Rev. A **4**, 579 (1971).
[59] J. Geiger, Z. Phys. A **282**, 129 (1977).
[60] W. R. Johnson, K. T. Cheng, K.-N. Huang, and M. Le Dourneuf, Phys. Rev. A **22**, 989 (1980).
[61] R. D. Knight, Phys. Rev. A **34**, 3809 (1986).
[62] K. Ueda, Phys. Rev. A **35**, 2484 (1987).
[63] K. Ueda, J. Opt. Soc. Am. B **4**, 424 (1987).
[64] A. L'Huillier, X. Tang, and P. Lambropoulos, Phys. Rev. A **39**, 1112 (1989).
[65] M. J. J. Vrakking, J. Phys. Chem. A **101**, 6761 (1997).
[66] F. Merkt and H. Schmutz, J. Chem. Phys. **108**, 10033 (1998).
[67] M. Schäfer, M. Andrist, H. Schmutz, F. Lewen, G. Winnewisser, and F. Merkt, J. Phys. B **39**, 831 (2006).
[68] A. Osterwalder and F. Merkt, Phys. Rev. Lett. **82**, 1831 (1999).
[69] C.-M. Lee and K. T. Lu, Phys. Rev. A **8**, 1241 (1973).
[70] J.-Q. Sun, Phys. Rev. A **40**, 7355 (1989).
[71] G. Racah, Phys. Rev. **61**, 537 (1942).
[72] S. D. Rosner, T. D. Gaily, and R. A. Holt, Phys. Rev. Lett. **40**, 851 (1978).
[73] M. Aymar, O. Robaux, and C. Thomas, J. Phys. B **14**, 4255 (1981).
[74] E. U. Condon and G. H. Shortley, *The Theory of Atomic Spectra* (Cambridge University Press, Cambridge, 1953).
[75] C. H. Greene and C. Jungen, Adv. At. Mol. Phys. **21**, 51 (1985).
[76] H. J. Wörner, M. Grütter, E. Vliegen, and F. Merkt (unpublished).
[77] R. N. Zare, *Angular Momentum* (Wiley, New York, 1988).
[78] C. M. Lee, Phys. Rev. A **10**, 584 (1974).
[79] A. R. Edmonds, J. Picart, N. T. Minh, and R. Pullen, J. Phys. B **12**, 2781 (1979).
[80] N. B. Delone, S. P. Goreslavsky, and V. P. Krainov, J. Phys. B **27**, 4403 (1994).
[81] V. B. Berestetskii, E. M. Lifshitz, and L. P. Pitaevskii, *Quantum Electrodynamics*, 2nd ed. (Butterworth-Heinemann, Oxford, 1982).
[82] R. Guérout, C. Jungen, H. Oueslati, S. C. Ross, and M. Telmini, Phys. Rev. A **79**, 042717 (2009).
[83] D. Brinkmann, Helv. Phys. Acta **41**, 367 (1968).
[84] N. J. Stone, At. Data Nucl. Data Tables **90**, 75 (2005).
[85] K. Harth, J. Ganz, M. Raab, K. T. Lu, J. Geiger, and H. Hotop, J. Phys. B **18**, L825 (1985).
[86] K. Harth, M. Raab, and H. Hotop, Z. Phys. D **7**, 213 (1987).
[87] K. Ito, K. Ueda, T. Namioka, K. Yoshino, and Y. Morioka, J. Opt. Soc. Am. B **5**, 2006 (1988).
[88] J. M. Weber, K. Ueda, D. Klar, J. Kreil, M.-W. Ruf, and H. Hotop, J. Phys. B **32**, 2381 (1999).